Precision Stark spectroscopy of the fine structure of the microwave transition $37P-37S$ in sodium Rydberg atoms

I. M. Beterov and I. I. Ryabtsev*
Institute of Semiconductor Physics, Siberian Branch of the Russian Academy of Sciences, 630090 Novosibirsk, Russia

(Submitted 19 November 1998)
Pis'ma Zh. Éksp. Teor. Fiz. **68**, No. 12, 853–857 (25 December 1998)

The results of experimental and theoretical investigations of the fine structure of the spectrum of the microwave transition $37P-37S$ in sodium Rydberg atoms in a weak electric field are reported. New data are obtained on the experimental values of the scalar and tensor polarizabilities of the $37P$ level. A numerical simulation of the Stark diagram, taking into account the influence of the anticrossings of the Rydberg levels, is performed, and the results are found to be in good agreement with experiment. © *1998 American Institute of Physics.* [S0021-3640(98)00124-8]

PACS numbers: 32.10.Fn, 32.80.Rm, 32.60.+i, 32.30.Bv

Accurate values of the atomic constants, which determine the magnitude and character of the Stark shifts and splitting of the levels in a weak electric field, are required for experiments on precision microwave spectroscopy of Rydberg atoms. The unavoidable residual electric fields present in experimental setups cause broadening and shifting of resonances, and they determine the limiting resolution in spectroscopic measurements. This is especially important at high values of the principal quantum number, since the polarizabilities of Rydberg states grow as n^7 with increasing level number n. The large increase in the measurement accuracy of quantum defects that has been achieved in the last few years[1,2] makes it possible to perform accurate calculations of the Stark diagrams of Rydberg levels taking into account the effect of anticrossings and breakdown of the quadratic or linear approximations. For this reason, the experimental verification of such calculations is a topical problem for determining the range of applicability of the theory.

Our objective in the present work was to investigate experimentally and theoretically the spectrum of the microwave transition $37P-37S$ in sodium Rydberg atoms in a weak static electric field and to perform accurate measurements of the scalar and tensor polarizabilities of the $37P$ level. Knowledge of the polarizabilities is required to take account of the effect of parasitic electric fields in subsequent experiments on precision microwave spectroscopy of cold Rydberg atoms and in experiments with a Rydberg micromaser on the transition $37P-37S$. The Na S and P states possess large quantum defects (1.347 and 0.854, respectively), so that a quadratic Stark effect in weak fields is

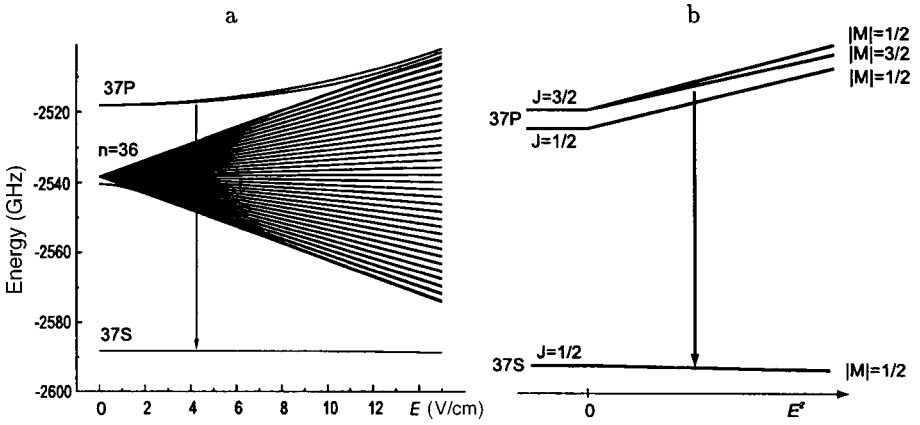

FIG. 1. a—Computed Stark diagram of Rydberg levels in Na atoms for states with $|M|=1/2$; b—scheme of the microwave transition $37P-37S$ in an electric field.

characteristic for these levels. The frequency shifts of the levels are described by the formula

$$\Delta\nu=-\frac{1}{2}\left\{\alpha_0+\alpha_2\frac{3M^2-J(J-1)}{J(2J-1)}\right\}E^2, \tag{1}$$

where α_0 and α_2 are the scalar and tensor polarizabilities, J and M are the total angular momentum of a given state and its projection on the electric field vector, and E is the electric field. We note that $\alpha_0=0$ for states with $J=1/2$, i.e., these levels do not split.

It turns out that as a result of the semiclassical nature of the motion of the outer electron in Rydberg atoms, it is possible to calculate numerically the transition dipole moments between Rydberg states[3] and the Stark diagrams of the energy levels for any value of the electric field. This can be done by diagonalizing the matrix of the interaction energy of an atom with the field.[4] We performed such calculations for levels near the transition $37P-37S$. As an example, Fig. 1a shows the computed Stark diagram of states with $|M|=1/2$. Similar diagrams were also constructed for states with $|M|=3/2$. According to Fig. 1a, for the $37P$ level the transition from the quadratic to the linear Stark effect occurs in a field of about 10 V/cm. The accuracy of the calculations is determined by the accuracy of the known values of the quantum defects, carefully measured in Ref. 1. The polarizabilities, calculated according to Fig. 1a, in a 2.86 V/cm field are presented in Table I. The computed values were used to construct the qualitative scheme of the transition $37P-37S$ in a weak electric field (Fig. 1b), making it possible to identify individual components of the observed spectrum taking account of the fine structure of the P states. A characteristic feature of the results is that because of the effect of anticrossings and the breakdown of the quadratic approximation the values of α_0 are different for the states $37P_{J=1/2}$ and $37P_{J=3/2}$.

In the experiments a beam of sodium atoms with temperature 500 K was allowed to effuse into a vacuum chamber. Excitation of the Rydberg states was accomplished with a three-step scheme $3S-3P-4S-37P_{J=1/2,3/2}$ under transverse illumination of the beam by three synchronized pulsed tunable lasers with a high pulse repetition rate (up to 10

TABLE I. Theoretical and experimental values of the scalar and tensor polarizabilities of the $37P$ level (in MHz/(V/cm)^2), measured at a static electric field of 2.86 V/cm.

	Theory		Experiment	
State	α_0	α_2	α_0	α_2
$37S_{1/2}$	3.7	0	-	-
$37P_{1/2}$	-107.2	0	-107 ± 5	0
$37P_{3/2}$	-113.8	13.2	-113 ± 5	13.3 ± 0.4

kHz). The tuning range of the laser at the last step made it possible to excite selectively the Rydberg P series of sodium with principal quantum numbers ranging from 11 to 50; the highest efficiency was reached for $n=35-37$. The characteristic frequencies of the single- and multiphoton transitions from these states lie in the range 50–100 GHz. Next, the beam of sodium Rydberg atoms was directed into the region of interaction with the resonant microwave radiation, generated by a backward wave tube and introduced from the open end of the waveguide into the space between two copper plates which produced a static electric field. The linewidth of the generator was 1 MHz, and the computed saturation intensity of the transition $37P-37S$ did not exceed several pW/cm^2. Transitions between fixed Rydberg states in an electric field were induced by scanning the frequency of the generator. This altered the initial populations of the levels. They were monitored by selective field ionization in a pulsed electric field. The electrons produced by ionization were detected with a vacuum channel multiplier, the signal from which was processed in a pulse counting mode in a CAMAC crate and a computer. To reduce the effect of thermal radiation, all elements of the detection system and the system for introducing the microwave radiation were cooled to liquid-nitrogen temperature. A detailed description of the experimental apparatus is given in Ref. 5.

Figure 2 shows the experimental traces of the spectrum of the transition $37P-37S$ in fields up to 5 V/cm. In the absence of a field, the spectrum consists of the two components $37S_{1/2}-37P_{1/2}$ and $37S_{1/2}-37P_{3/2}$, corresponding to the fine structure of the $37P(\Delta\nu=114$ MHz) level. The width (5 MHz) of the peaks was determined by the generator linewidth, transit-time and Doppler broadening (0.5 MHz), and field-induced broadening by the microwave field, whose contribution was dominant. It is difficult to give a quantitative description of the amplitudes of the peaks, since they depend on the transition dipole moments, which can be easily calculated, and on the relative orientations of the vectors of the static electric field, the microwave radiation, and the laser radiation at the third step as well as on the fluctuations of the lasing spectrum of this laser, which excites simultaneously both components of the fine structure of the $37P$ level. In our experiments the polarization vectors of the microwave and laser radiations were all oriented in the same direction and were perpendicular to the static electric field, so that predominantly transitions with $\Delta M=\pm1$ were excited.

When a static electric field was applied, the resonances shifted and the component $37S_{1/2}-37P_{3/2}$ split into the two components $37S_{1/2,|M|=1/2}-37P_{1/2,|M|=1/2}$ and $37S_{1/2,|M|=1/2}-37P_{1/2,|M|=3/2}$, the ratio of whose amplitudes was in good agreement with the theory of angular momentum (1/3 for $P-S$ transitions). As the electric field increased, the amplitude of the first component decreased to zero. This is probably due to a change

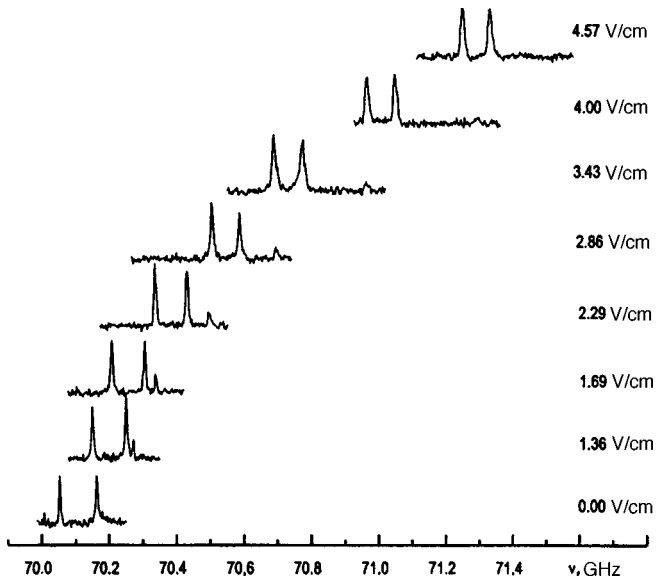

FIG. 2. Experimental trace of the spectrum of the microwave transition $37P-37S$ in sodium Rydberg atoms at different values of the static electric field.

in the transition probabilities and mixing of the Rydberg states in an electric field. Measurement of the dependence of the shift of each component of the spectrum in Fig. 2 confirmed closeness to the quadratic regime in fields up to 3 V/cm. When the electric field was increased above 5 V/cm, an appreciable deviation (about 10%) from the quadratic law appeared. The experimental values of the scalar and tensor polarizabilities of the $37P$ level measured in a 2.86 V/cm field are presented in Table I. Comparing with the calculations shows good agreement with experiment. The accuracy of the measurements was determined mainly by the spatial nonuniformity of the static electric field in the interaction region. It led to broadening of up to 15 MHz, observed in a 4.86 V/cm field, of the resonances. The nonuniformity of the field can be approximately calculated using Eq. (1) and is less than 30 mV/cm (0.6%).

The results obtained confirm the high accuracy of the numerical calculations of the Stark diagrams of Rydberg levels performed by diagonalizing the matrix of the interaction of a Rydberg electron with a static electric field. New data on the polarizabilities will make it possible to refine the values of the critical fields for the double Stark resonance, which we observed, on the two-photon transition $36P-37P$ (Ref. 5). A further increase in accuracy is planned in experiments with cold Rydberg atoms. Possible applications are the absolute calibration of a weak electric field in vacuum according to measurements of the Stark shifts of the microwave transition frequencies as well as the possibility of measuring small values of the spatial nonuniformities of electric fields according to the broadening of the resonances, which is an important problem for a variety of spectroscopic investigations.

This work was supported by grants from the Russian Fund for Fundamental Research (Nos. 96-02-19041 and 97-02-18551).

*e-mail: ryabtsev@isp.nsc.ru

[1] S. F. Dyubko, M. N. Efimenko, V. A. Efremov, and S. V. Podnos, Kvant. Elektron. (Moscow) **22**, 946 (1995).
[2] M. Ciocca, C. E. Burkhardt, J. J. Leventhal, and T. Bergeman, Phys. Rev. A **45**, 4720 (1992).
[3] A. R. Edmonds, J. Picart, N. Tran-Minh, and R. Pullen, J. Phys. B **12**, 2781 (1979).
[4] L. Zimmerman, M. G. Littman, M. M. Kash, and D. Kleppner, Phys. Rev. A **20**, 2251 (1979).
[5] I. M. Beterov, A. O. Vyrodov, I. I. Ryabtsev, and N. V. Fateev, Zh. Éksp. Teor. Fiz. **101**, 1154 (1992) [Sov. Phys. JETP **74**, 616 (1992)].

Translated by M. E. Alferieff

Mechanism of rescattering of photoelectrons by the parent ion in the optical tunneling regime

S. P. Goreslavskiĭ* and S. V. Popruzhenko
Moscow Engineering-Physics Institute, 115409 Moscow, Russia

(Submitted 18 August 1998; resubmitted 26 November 1998)
Pis'ma Zh. Éksp. Teor. Fiz. **68**, No. 12, 858–863 (25 December 1998)

The interference structure of the angular distributions in the high-energy part of the above-threshold ionization spectrum is calculated. The components of the wave packet of the ionized electron that interfere with one another during the interaction with the parent ion are identified. It is shown that the angular distribution averaged over the interference oscillations is determined mainly by the angular dependence of the effective interaction time. © *1998 American Institute of Physics.* [S0021-3640(98)00224-2]

PACS numbers: 34.80.Kw, 34.80.Dp, 33.60.−9

Investigations performed in the last few years have shown that in a linearly polarized laser field the spectrum of photoelectrons detected in a definite direction consists of two parts with different properties. The initial section, which is explained by direct (produced by the laser alone) above-threshold ionization is followed by a plateau which arises in the course of the interaction (rescattering) of the electrons, injected into the continuum and accelerated by the laser field, with the parent ion (see the reviews in Refs. 1 and 2). The two-component structure is most pronounced in the tunneling limit.[3] Quantum interference effects, recently observed experimentally,[4] in the low-energy part of the spectrum naturally prompt the analogous question for distributions on the plateau. A calculation with a zero-range model potential[5] showed that in the tunneling limit in the presence of an extended plateau, the alternation of dips and peaks that is typical of interference is observed in the spectrum along a fixed direction at all energies. The low-energy picture is consistent with the concepts of a semiclassical analysis (by the method of stationary phase) of the direct ionization amplitude[4,6,7] as to the mechanism giving rise to the interference structure and the parameters of that structure. A similar comparison was not made on the plateau because of the lack of semiclassical expressions for the amplitude for ionization with rescattering. Also, as far as we know, the interference structure of the angular distributions on the plateau under conditions of the tunneling regime has not been described in the literature, either.

We report below the main results of a semiclassical analysis of the ionization amplitude with rescattering that reveal the interference mechanism in the spectral-angular distributions of photoelectrons with energies in the region of a developed plateau, and we show that the angular distributions at such energies have the same distinct interference structure as the energy spectra in Ref. 5.

We solve the nonstationary Schrödinger equation for an atom in a laser field, assuming that before the field is switched on, the atom is in a bound state $\psi_0(\mathbf{r},t)=\psi_0(\mathbf{r})\exp(iIt)$ with ionization potential I. We seek the solution in the form $\Psi=\psi_0(\mathbf{r},t)+\chi(\mathbf{r},t)$, where the new unknown function $\chi(\mathbf{r},t)$ satisfies an inhomogeneous equation in which the source is proportional to the initial state $\psi_0(\mathbf{r},t)$ and does not depend on the atomic potential. It is convenient to change to the momentum representation, setting

$$\chi(\mathbf{r},t)=\sum_{\mathbf{p}} C(\mathbf{p},t)\Psi_{\mathbf{p}}(\mathbf{r},t),$$

where

$$\Psi_{\mathbf{p}}(\mathbf{r},t)=\exp\left\{ i\mathbf{p}\cdot\mathbf{r}-i\int_{-\infty}^{t} d\tau\epsilon_{\mathbf{p}}(\tau)\right\}$$

is a nonrelativistic Volkov state. Here and below the following notation is employed: $\hbar=m=-e=1$; $\mathbf{p}$ is the canonical momentum; $\epsilon_{\mathbf{p}}(t)=(\mathbf{p}+\mathbf{p}_F(t))^2/2$ is the kinetic energy of an electron in a linearly polarized laser field $\mathbf{F}(t)=F\{\sin\omega t,0,0\}$ with the vector potential $\mathbf{p}_F(t)=p_F\{\cos\omega t,0,0\}$, where $p_F=F/\omega$; and, $U_p=F^2/4\omega^2$ is the ponderomotive potential. In the inhomogeneous integrodifferential equation for $C(\mathbf{p},t)$ the Fourier transform $V(\mathbf{q})$ of the atomic potential occurs only in the integrand. Treating the integral term as a perturbation, we find a solution in the form of a series in powers of the atomic potential $C(\mathbf{p},t)=C^{(0)}(\mathbf{p},t)+C^{(1)}(\mathbf{p},t)+\ldots$.[8] The solution $C^{(0)}(\mathbf{p},t)$ is a time integral of the source (the inhomogeneity), and its maximum value $C^{(0)}(\mathbf{p},\infty)$ is identical to the ionization amplitude in the Keldysh–Faisal–Reiss (KFR) model.[9] The contribution from the first iteration is obtained in the form

$$iC^{(1)}(\mathbf{p},\infty)=\int_{-\infty}^{+\infty} dt\Psi^{*}_{\mathbf{p}}(0,t)\int d^3kV(\mathbf{p}-\mathbf{k})\Psi_{\mathbf{k}}(0,t)C^{(0)}(\mathbf{k},t) \tag{1}$$

and it has a simple interpretation — it is the scattering amplitude, calculated in first-order perturbation theory in the atomic potential, of the coherent packet, formed by ionization, of the Volkov states $\chi^{(0)}(\mathbf{r},t)=\Sigma_{\mathbf{k}}C^{(0)}(\mathbf{k},t)\Psi_{\mathbf{k}}(\mathbf{r},t)$ in the final Volkov state $\Psi_{\mathbf{p}}(\mathbf{r},t)$. The properties of the packet $\chi^{(0)}(\mathbf{r},t)$ are described in Ref. 8. If an individual Volkov wave is substituted as the initial state, expression (1) is identical to the induced bremsstrahlung amplitude in the Born approximation.[10]

We shall confine our attention to the tunneling regime of ionization ($\gamma=\omega(2I)^{1/2}/F<1$; $\omega<I$, $F<F_a=(2I)^{3/2}$) and we shall calculate expression (1) using the zeroth-order solution obtained in Ref. 8 under these conditions

$$C^{(0)}(\mathbf{p},t)=\frac{i}{\sqrt{2\pi}}\int_{-\infty}^{t} dt_0F^{3/2}(t_0)\,\delta(\dot{\epsilon}_{\mathbf{p}}(t_0))\exp\left\{ i\Phi(\mathbf{p},t_0)-\frac{F_a}{3F(t_0)}\left[1+\frac{3\epsilon_{\mathbf{p}}(t_0)}{2I}\right]\right\}, \tag{2}$$

where

$$\Phi(\mathbf{p},t)=It+\int_{-\infty}^{t} d\tau\epsilon_{\mathbf{p}}(\tau).$$

The delta function in Eq. (2) shows that the transition into a state with momentum $\mathbf{p}$ occurs instantaneously at the times t_0 such that $\nu_x(t_0)=p_x+p_F\cos\omega t_0=0$. The instantaneous character of the transition is an idealization of the fact that the tunneling time is a small fraction of one optical period. The velocity $\nu_x(t_0)$ vanishes twice during each optical cycle, and the contributions of these two points interfere in the direct-ionization amplitude. We note that at the indicated times the laser field is directed in opposite directions.

Since we are interested in the amplitude (1) in the region of the plateau, where $\epsilon=p^2/2>(2-3)U_p$, we set $V(\mathbf{p}-\mathbf{k})\approx V(p)$, since the scattered packet contains primarily states with low energies $k^2/2\ll(2-3)U_p$. Then, with the delta function taken into account, the momentum integration in Eq. (1) can be performed analytically, and the remaining integral over two times can be calculated by the stationary-phase method, since the phase of the integrand is proportional to $z_F=4U_p/\omega\gg1$. Taking account of only the real stationary points, the conditions of stationarity

$$(\varphi_s-\varphi_0)\cos\varphi_0-\sin\varphi_s+\sin\varphi_0=0, \tag{3}$$

$$\epsilon_{\mathbf{p}}(\varphi_s)=\epsilon_{\mathbf{k}(\varphi_0)}(\varphi_s) \tag{4}$$

are identical to the well-studied equations of the classical rescattering model.[11] In Eq. (4), $\mathbf{k}(\varphi_0)=-p_F\{\cos\varphi_0,0,0\}$.

The two equations (3) and (4) implicitly couple four quantities: the energy of the detected electron $\epsilon=p^2/2$, the angle of emergence measured from the polarization direction θ, and the real variables $\varphi_0=\omega t_0$ and $\varphi_s=\omega t_s$, which are the moments of ionization and scattering, respectively.

Since $\epsilon(\varphi_0,\theta)=\epsilon(\varphi_0+2\pi,\theta)$ and $\epsilon(\varphi_0,\theta)=\epsilon(\varphi_0+\pi,\pi-\theta)$, which follow from Eqs. (3) and (4), it is sufficient to consider the function $\epsilon=\epsilon(\varphi_0,\theta)$ in one half period. We choose the interval $0<\varphi_0<\pi$, where the field is maximum at the time $\varphi_0=\pi/2$. For any φ_0 in the interval $\pi/2<\varphi_0<\pi$, Eq. (3) possesses a discrete sequence of roots $\varphi_s=\varphi_s(\varphi_0)$, which, generally speaking, correspond to several successive returns of the ionized electron to the parent atom. Since the contribution of the later returns to the amplitude (1) decreases rapidly because of the spreading of the wave packet of the photoelectron, in what follows we shall mean only the first return. Returns are impossible for $0<\varphi_0<\pi/2$. Thus, the function $\epsilon=\epsilon(\varphi_0,\theta)$ is defined only in the second quarter of the half period under consideration, where, as one can see from Fig. 1, it has an isolated maximum. The magnitude $10U_p$ of this maximum for $\theta=0$ is the known upper limit of the rescattered electron spectrum in the classical model. From the existence of a maximum of the function $\epsilon=\epsilon(\varphi_0,\theta)$ it follows immediately that the inverse function $\varphi_0=\varphi_0(\epsilon,\theta)$ required to obtain the ionization amplitude (1) is double-valued. In other words, two stationary points (φ_{01} and φ_{02} in Fig. 1), corresponding to ionization in the direction θ with energy ϵ, are present in one quarter of the period. The contributions of these stationary points interfere in the transition amplitude (1). We note that the interfering waves are injected into the continuum and interact with the ion at different (but quite close) times.

The ionization rate is proportional to $|C^{(0)}(\mathbf{p},\infty)+C^{(1)}(\mathbf{p},\infty)|^2$, but since on the plateau $|C^{(1)}|\gg|C^{(0)}|$, it is sufficient to retain only $C^{(1)}$. Then, in the presence of two

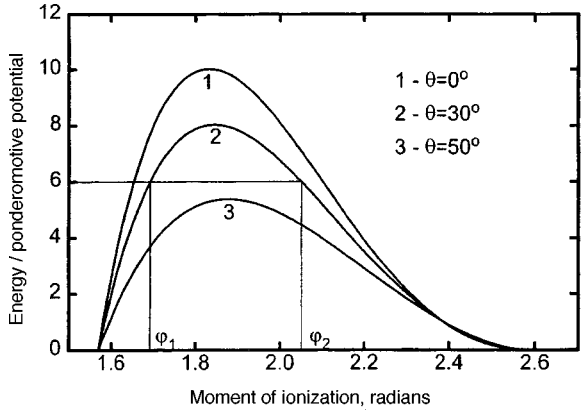

FIG. 1. Energy $\epsilon=\epsilon(\varphi_0,\theta)$ of an ionized electron as a function of the moment of ionization $\varphi_0=\omega t_0$, calculated from Eqs. (3) and (4). Curves *1*, *2*, and *3* correspond to the directions of emergence $\theta=0°$, 30°, and 50°. The contributions of the stationary points φ_{01} and φ_{02} interfere in amplitude for ionization with energy $\epsilon=6U_p$ at the angle $\theta=30°$.

stationary points, the spectral-angular distribution $w_{\rm resc}(\epsilon,\theta)\equiv dW_{\rm resc}/d^3p$ of the rescattered photoelectrons has the form

$$w_{\rm resc}(\epsilon,\theta)=w_1+w_2+2\sqrt{w_1w_2}\cos S_{12}, \tag{5}$$

where the contribution of an individual stationary point (the index is dropped) is

$$w=\frac{\omega^2V^2(p)}{(2\pi)^4F(\varphi_0)(\varphi_s-\varphi_0)^3}\tau_{\rm resc}^2(\epsilon,\theta)\exp\left\{-\frac{2F_a}{3F(\varphi_0)}\right\} \tag{6}$$

and the phase difference between the stationary points is

$$\omega S_{12}(\mathbf{p})=I(\varphi_{02}-\varphi_{01})+\int_{\varphi_{s1}}^{\varphi_{s2}}d\varphi\,\epsilon_{\mathbf{p}}(\varphi)-\int_{\varphi_{02}}^{\varphi_{s2}}d\varphi\,\epsilon_{\mathbf{k}(\varphi_{02})}(\varphi)+\int_{\varphi_{01}}^{\varphi_{s1}}d\varphi\,\epsilon_{\mathbf{k}(\varphi_{01})}(\varphi). \tag{7}$$

The exponential factor in Eq. (6) was also obtained in Ref. 12.

In Eq. (6) the factors corresponding to the concepts which are used in the classical rescattering model can be identified in an obvious way: the probability of direct ionization (proportional to the tunneling exponential); the elastic scattering cross section of the atomic potential (in the Born approximation $\propto V^2(\mathbf{p})$); and, finally, the factor $(\varphi_s-\varphi_0)^{-3}$ describing the spreading of the wave packet of an ionized electron over the time from the moment of ionization up to the first return to the atom. However, besides these factors, the probability (6) also contains the factor

$$\tau_{\rm resc}^2=z_F^{-1}\left|\sin\varphi_s\left(\sqrt{2\epsilon/U_p}\cos\theta+\cos\varphi_0\right)\right|^{-1}. \tag{8}$$

The interaction time $\tau_{\rm resc}$ is essentially determined by s quantum parameter (in ordinary units $z_F=4U_p/\hbar\omega$) and is the size of the effective region of integration near the stationary point, i.e., the time interval during which the energies are resonantly close to one another as prescribed by the relation (4).

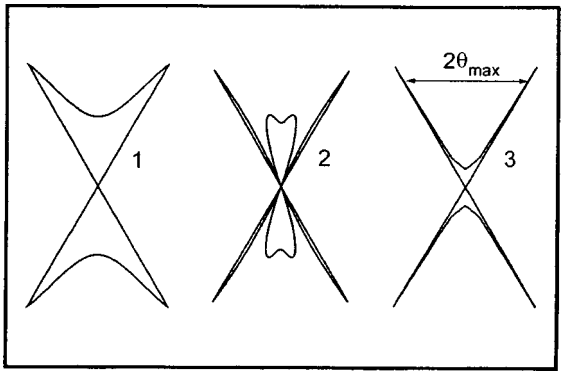

FIG. 2. Angular distributions of photoelectrons with energy $\epsilon = 8U_p$, calculated from Eqs. (5)–(8). The field is polarized in the vertical direction. Curves: *1* — neglecting and *2* — taking account of the interference term in (5); *3* — result of the classical model.[11] The distributions are normalized to the maximum value; the absolute dimensions of the curve *2* are half of those of curve *1*. The parameters correspond to ionization of Xe ($I = 12.1$ eV) by TiSa laser radiation ($\hbar\omega = 1.58$ eV) with intensity 2.15×10^{14} W/cm^2 ($\gamma = 0.77$, $z_F = 25$ and $F/F_a = 0.085$).

The angular distribution, calculated from the relations (5)–(8), of electrons with energy $\epsilon = 8U_p$ is displayed in Fig. 2 (curve *2*). If complex stationary points are ignored, then this distribution, just as in the classical model (curve *3*, Fig. 2), is cut off abruptly for $\theta > \theta_{\max}(\epsilon)$. Comparing with the continuous curve *1*, obtained using the same formulas but without the last term in Eq. (5), in Fig. 2 shows that the deep dips are due to interference.

The stationary points in the calculations performed were treated as isolated. This assumption breaks down at all angles in the range $0 < \theta < \theta_{\max}(\epsilon)$ as $\epsilon \to 10U_p$, and for angles $\theta \to \theta_{\max}(\epsilon)$ it breaks down at intermediate energies. In consequence, τ_{resc} calculated directly from Eq. (8) increases without bound as $\theta \to \theta_{\max}(\epsilon)$. To construct the curves *1* and *2* in Fig. 2, the distribution near the limiting angle was calculated by a modified stationary-phase method, retaining the third derivative in the expansion of the phase.

The distribution changes as the energy decreases to low values: The limiting angle increases and the number of interference bumps increases. The phase difference (7) has the form $S_{12} = z_F \Delta_{12}(\epsilon/U_p, \theta)$, where $z_F \gg 1$, and $\Delta_{12}(\epsilon/U_p, \theta)$ is a continuous function of the order of 1. Specifically, as ϵ varies from $4U_p$ to $10U_p$, $\Delta_{12}(\epsilon/U_p, 0)$ decreases to 0 approximately linearly from a value close to 1. The phase difference as a function of angle changes from zero as $\theta \to \theta_{\max}$ to the maximum value $S_{12}(\epsilon/U_p, 0)$ at $\theta = 0$. For this reason, the number of interference bumps in the angular distribution at fixed energy will be $z_F(\epsilon, \theta = 0)/\pi$. As was reported at one of the latest conferences, an interference structure in the angular distributions also arises in calculations with the Coulomb–Volkov states.[13]

In experiments the interference pattern is smoothed out by the space–time nonuniformity of the laser field. For this reason, it is helpful to discuss the distribution averaged over the interference oscillations, $\overline{w} = w_1 + w_2$. This is the distribution (Fig. 2, curve *1*) that should be compared with the classical model, which in principle does not describe

interference (Fig. 2, curve *3*). It is obvious that instead of a deep dip at $\theta=0$, as predicted by the classical model, the averaged distribution calculated from Eq. (6) is smooth and has a flat minimum in the direction of polarization. The measurements of the angular distributions on a developed plateau[2] attest to a uniform distribution. Analysis shows that the form of $\overline{w}$ in the interval $0<\theta<\theta_{\max}(\epsilon)$ is determined mainly by the angular dependence of the collision time τ_{resc} (8). The Fourier transform of the atomic potential in Eq. (6) depends only on the electron energy and has no effect on the form of the angular distributions.

The optimal conditions for observing experimentally the interference structure in angular distributions are satisfied at electron energies near the top limit of the plateau, where interference dips already exist but remain small in number. In order for the degree of modulation of the distributions to be high, the interfering amplitudes should not differ much. In the same laser field F the tunneling exponentials at the times φ_{01} and φ_{02} will be closer to one another for atoms with a weaker atomic field $F_a=(2I)^{3/2}$, i.e., with a lower ionization potential. A picture similar to curve *2* in Fig. 2 can be expected under the experimental conditions of Ref. 14, but at a radiation intensity 1.5–2 times higher than in the published data.

In conclusion, we note that the semiclassical quantum model formulated above for the formation of the high-energy part of the above-threshold ionization spectrum retains the simplicity and physical transparency of the classical picture, and it remains quite convenient for analyzing experiments on photoionization by high-intensity laser radiation.

We thank W. Becker, N. B. Delone, V. P. Kraĭnov, and M. V. Fedorov for stimulating discussions. This work was supported by the Russian Fund for Fundamental Research (Projects 96-02-18299 and 97–02-16973).

*e-mail: grslv@theor.mephi.msk.su

[1] W. Becker, A. Lohr, and M. Kleber, Quantum Semiclassic. Opt. **7**, 423 (1995).
[2] N. B. Delone and V. P. Kraĭnov, Usp. Fiz. Nauk **168**, 531 (1998).
[3] B. Sheehy, B. Walker, R. Lafon *et al.*, in *Inst. Phys. Conf. Ser. No. 154*, edited by P. Lombropolus and H. Walther, 1996, p. 106.
[4] G. G. Paulus, F. Zacher, H. Walther *et al.*, Phys. Rev. Lett. **80**, 484 (1998).
[5] A. Lohr, M. Kleber, R. Kopold *et al.*, Phys. Rev. A **55**, R4003 (1997).
[6] A. M. Perelomov, V. S. Popov, and M. V. Terent'ev, Zh. Éksp. Teor. Fiz. **50**, 1393 (1966) [Sov. Phys. JETP **23**, 924 (1966)].
[7] M. Lewenstein, K. C. Kulander, K. J. Schafer *et al.*, Phys. Rev. A **51**, 1495 (1995).
[8] S. P. Goreslavskii and S. V. Popruzhenko, Laser Phys. **8** (5), 1013 (1998).
[9] L. V. Keldysh, Zh. Éksp. Teor. Fiz. **47**, 1945 (1964) [Sov. Phys. JETP **20**, 1307 (1965)]; F. H. M. Faisal, J. Phys. B: At. Mol. Phys. **6**, L89 (1973); H. R. Reiss, Phys. Rev. A **22**, 1786 (1980).
[10] F. V. Bunkin and M. V. Fedorov, Zh. Éksp. Teor. Fiz. **49**, 1215 (1965) [Sov. Phys. JETP **22**, 844 (1966)].
[11] G. G. Paulus, W. Becker, W. Nicklich *et al.*, J. Phys. B: At. Mol. Opt. Phys. **27**, L703 (1994).
[12] V. P. Krainov and M. B. Smirnov, in *Seventh International Workshop on Laser Physics*, Berlin, Germany, July 6–10, 1998, Program and Book of Abstracts, Vol. 1.
[13] D. B. Milosevic and F. Ehlotzky, *ibid.*
[14] L. D. Van Woerkom, P. Hansch, and M. A. Walker, in *Inst. Phys. Conf. Ser. No. 154*, edited by P. Lombropolus and H. Walther, 1996, p. 78.

Translated by M. E. Alferieff

New ferromagnetic compound $CaCo_2$ (C15) synthesized at high pressure

A. V. Tsvyashchenko, L. N. Fomicheva, M. V. Magnitskaya, and V. A. Sidorov
L. F. Vereshchagin Institute of High-Pressure Physics, Russian Academy of Sciences, 142092 Moscow, Russia

A. V. Kuznetsov and D. V. Eremenko
Moscow Engineering-Physics Institute, 115409 Moscow, Russia

V. N. Trofimov
Nuclear Laboratory, Joint Institute for Nuclear Research, 141980 Dubna, Russia

(Submitted 3 November 1998)
Pis'ma Zh. Éksp. Teor. Fiz. **68**, No. 12, 864–869 (25 December 1998)

The compound $CaCo_2$ with the C15 cubic Laves phase structure and an estimated density of 5.21 g/cm^3 has been synthesized at 8.0 GPa pressure. Magnetization measurements showed that the compound $CaCo_2$ is a ferromagnet with Curie temperature 528 K and magnetic moment per Co atom $1.75\mu_B$ at $T=4.2$ K. LMTO calculations of the electronic band structure showed that $CaCo_2$ forms as a result of an $s-d$ electronic transition of Ca and in the ground state it is a ferromagnet with a high magnetic moment per Co atom. © *1998 American Institute of Physics.* [S0021-3640(98)00324-7]

PACS numbers: 75.50.Cc, 75.60.Ej

Interest in the high-pressure synthesis of a new class of alloys and intermetallic compounds, which are not formed at normal pressure, of alkali metals with *d* transition metals has increased sharply in the last three years.[1–3] Interest is being shown especially in the high-pressure formation of new magnetic compounds and alloys in the system K–Ni.[4] It is expected that these investigations will explain the low density of the earth's core, which consists mainly of iron-group metals.[5,6] Potassium is one of the light elements that could be present in the earth's core, since it is generally agreed that the constant internal heat source of the earth is radioactive decay of U, Th, and ^{40}K. However, it should be noted that ^{40}K can be formed in large quantities only as a result of the known nuclear reaction of calcium (^{40}Ca) with neutrons after spontaneous fission of U (^{40}Ca$\{n,p\}^{40}$K). For this reason, we believe that to explain the low density of the earth's core it is no less important and promising to study the formation of alloys and compounds of calcium with $3d$ transition metals

Indeed, alkaline-earth metals (Ca, Sr, Ba), like the alkali metals (K, Rb, Cs), undergo an $s-d$ electronic transition under high pressure, as a result of which they can be treated as analogs of the corresponding *d*-transition metals.[7–11] As a result, the formation

of their compounds with $3d$ transition metals becomes possible. At the same time, according to its chemical activity Ca is the analog of the anomalous divalent rare-earth metal ytterbium (Yb), whose electronic configuration also changes at 4 GPa from $4f^{14}6s^2$ to $4f^{13}5d^16s^2$ (Ref. 12), and, as a result, new compounds with Fe and Mn are formed at high pressure.[13–15]

For this reason, to study the formation of new compounds and alloys of calcium with $3d$ transition metals at high pressure we employed a method which we developed for synthesizing compounds and alloys of ytterbium with $3d$ transition metals.[16,17] We also investigated some magnetic properties of the compound $CaCo_2$, which we synthesized, and we performed the first microscopic calculations of the electronic structure.

Experimental procedure and results. The synthesis experiments were performed in a chamber of the ''Toroid'' type[18] at 8.0 GPa. Heating up to the melting temperature was accomplished by passing a current through a sample placed inside a tube made of a single crystal of potassium chloride. The details of the synthesis are described in Ref. 16. Cylindrical samples with a mass of 0.4 g were prepared by compressing a mixture of the powders of the initial components in a medium consisting of spectroscopically pure argon. Electrolytic calcium powder (99.95) was prepared from an ingot in a medium of spectroscopically pure argon using a hard-alloy tool. The manganese, iron, cobalt, and nickel powders were 99.9% pure. The compounds were synthesized for the composition CaT_2, where T = Mn, Fe, Co, and Ni, since the formation of compounds at this composition is most likely.[19] The structure and phase composition of the samples obtained were investigated by x-ray diffraction, by obtaining Debye powder patterns (RKU-114 camera), and by obtaining diffraction patterns (DRON-2 diffractometer).

The x-ray investigations of Ca–Mn and Ca–Fe samples showed that the formation of compounds with the composition CaT_2 is not observed in these systems at pressures up to 8.0 GPa. The formation of the compounds $CaCo_2$ and $CaNi_2$ was observed in the systems Ca–Co and Ca–Ni. These compounds crystallize in a C15 cubic Laves phase structure ($MgCu_2$ type) with the space group O_h^7–$Fd3m$, $Z=8$. The unit cell parameter of $CaCo_2$ is $a=7.412\pm0.005$ Å, and the density calculated from the x-ray data is $\rho=5.21$ g/cm^3. The formation of the compound $CaCo_2$ was not observed at synthesis pressure 6.0 GPa. The compound $CaNi_2$ possesses a unit cell parameter $a=7.246\pm0.007$ Å. This value is the same as the cell parameter of the compound $CaNi_2$ synthesized at normal pressure.[20]

Measurements of the magnetization of polycrystalline samples of the compound $CaCo_2$ synthesized at 8.0 GPa were performed at normal pressure with a SQUID magnetometer[21] in the temperature range 4.2–300 K and in external magnetic fields up to 0.9 T. The magnetic ordering temperature was determined by an induction method.[22] Measurements above room temperature were performed in polysiloxane liquid (PÉS-5).

Figure 1 shows the magnetization in an external field at temperature 4.2 K. Figure 2 shows the temperature dependence of the magnetization of the sample in an external field 0.01 T, and the inset shows the temperature dependence of the susceptibility.

The measurements of the magnetic property showed that the compound $CaCo_2$ is a ferromagnet with Curie temperature 528 K. The magnetic moment $T=4.2$ K in a 0.9 T external magnetic field is $\mu=3.5\mu_B$/f.u. If it is assumed that a magnetic moment is not induced on the Ca ion, then the magnetic moment per Co ion is $1.75\mu_B$. Thus the

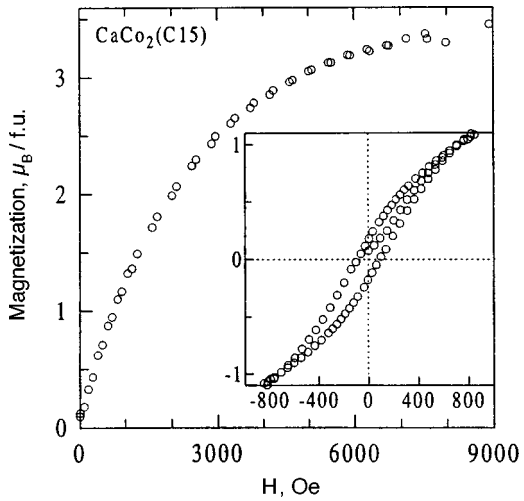

FIG. 1. Magnetization of $CaCo_2$ in an external field at $T=4.2$ K.

observed magnetic moment per Co ion in the compound $CaCo_2$ is slightly greater than the magnetic moment in metallic Co, where it equals $1.715\mu_B$.[23]

Calculations of the electronic band structure and discussion of the results. It is well known[24] that the collectivized-electron model is now universally accepted for $3d$ magnets, and it is widely used to describe the magnetic properties of the ground state of $3d$ metals, alloys, and intermetallides. A specific manifestation of the itinerant nature of the magnetism is the metamagnetism of collectivized electrons,[25] where in a magnetic field (external or effective) the paramagnetic system of itinerant electrons transforms abruptly into the ferromagnetic state. The well-studied compounds RCo_2 (R denotes a

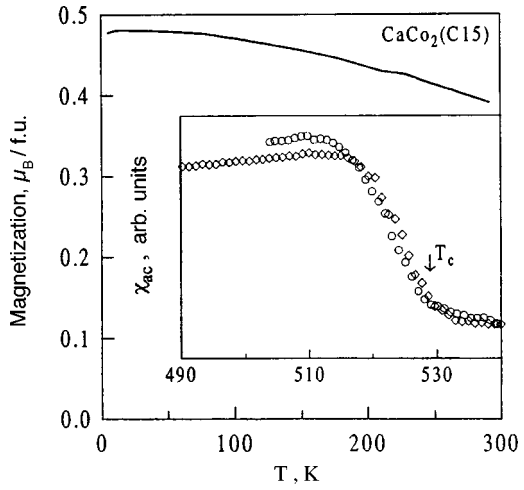

FIG. 2. Temperature dependence of the magnetization of $CaCo_2$ in a 0.01 T external field. The inset shows the temperature dependence of the susceptibility above room temperature.

trivalent rare-earth element), which, like the new compound $CaCo_2$, crystallize in the cubic Laves phase structure, also possess this property. Thus for the metamagnetic compounds $LuCo_2$ and YCo_2, where R is a nonmagnetic element, the paramagnetic state (PM) is stable and the $3d$ moment is zero.[24] In this connection, it is important to perform first-principles calculations of the electronic structure for the compound $CaCo_2$ with a stable ferromagnetic state in order to understand the nature of its magnetism.

The calculations were performed on the basis of the density functional theory[26] by a variational method using linearized MT orbitals (LMTO).[27] We used a generalization of the LMTO method[28] that does not contain the restrictive assumption of a spherically symmetric crystal potential. The exchange–correlation potential was treated in the local spin density approximation.[29] The electronic density of states (EDS) $N(E)$ was determined by the method of tetrahedra on a set of about 150 **k** points. The calculations were performed for the paramagnetic (PM) and ferromagnetic (FM) states of $CaCo_2$ with the experimental lattice parameter $a=7.412$ Å. For comparison, calculations were also performed for pure Ca and Co.

Comparing the computed total energy E_{tot} for the PM and FM states of $CaCo_2$ showed that for the experimental value of the lattice parameter E_{tot} for the FM state is 0.03 Ry/f.u. lower than the total energy for the PM state. The high peak in the EDS at the Fermi level in the PM state $N(E_F)=201.0$ states/(Ry·f.u.) in the spin-polarized calculation splits, and $N(E_F)$ decreases to 62.6 states/(Ry·f.u.) in the FM state (Fig. 3). We estimated the Stoner criterion k of ferromagnetism for $CaCO_2$. In the PM state the d-electron density at the cobalt atom is $N_d^{\text{Co}}(E_F)=97.6$ states/(Ry·atom) is two orders of magnitude greater than all other partial EDSs. Therefore it can be assumed that $k=2J_{dd}[N_d^{\text{Co}}(E_F)]^2/N(E_F)$, where J_{dd} is the exchange integral for the d orbital of Co.[30] The value obtained $k=5.2$ is much greater than 1, which likewise attests to the stability of $CaCo_2$ in the FM state.

The computed values of the electron density ρ_{AS} at the surface of the atomic sphere (which in simple substances is identical to the Wigner–Seitz sphere), the partial numbers of electrons per formula unit, and the magnetic moments μ are given in Table I. It is evident from Table I that in the compound $CaCo_2\rho_{AS}$ for Ca and Co are comparable, i.e., in the compound the Ca atoms undergo strong compression and the Co atoms are stretched. In the compound the distance between the Ca atoms is $d_{\text{Ca–Ca}}=3.21$ Å. Exactly the same distance between atoms is observed in pure Ca at pressure 5.0 GPa,[31] i.e., a 5.0 GPa pressure can be treated as the minimum pressure at which the compound $CaCo_2$ can form. Indeed, experiments have shown that $CaCo_2$ does not form below 6.0 GPa.

TABLE I. Computed characteristics for Ca and Co atoms in the compound $CaCo_2$ compared with the values for pure Ca and Co.

Object	ρ_{AS}, r_B^{-3}	Z_s	Z_p	Z_d	Z	μ, μ_B/at.
fcc Ca	0.007	0.82	0.65	0.53	2.0	0
FM hcp Co	0.040	0.65	0.76	7.59	9.0	1.60
Ca in $CaCo_2$	0.017	0.54	0.59	0.83	1.96	−0.30
Co in $CaCo_2$	0.026	0.76	0.62	7.64	9.02	1.52

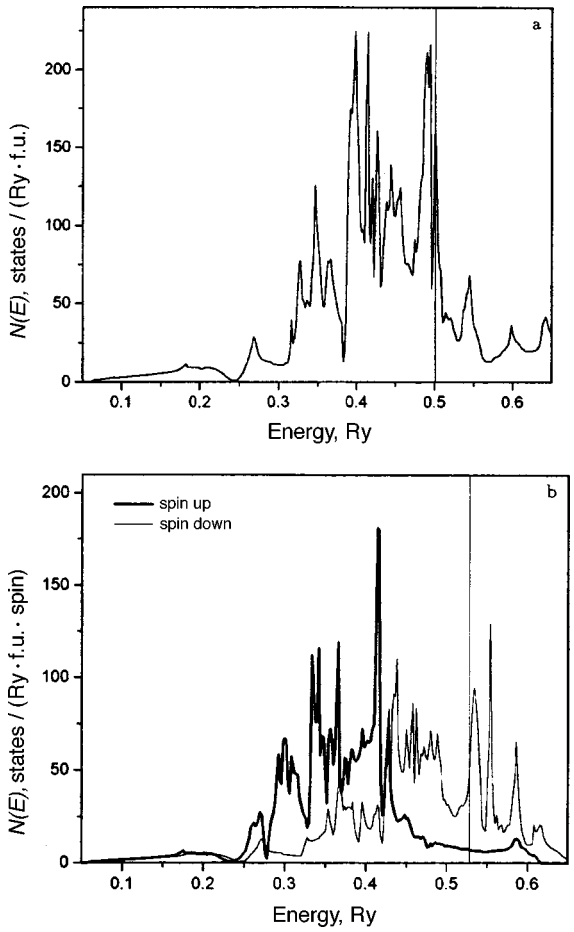

FIG. 3. Computed electron density of states $N(E)$ of paramagnetic (a) and ferromagnetic (b) $CaCo_2$. The vertical line shows the position of the Fermi level.

Calculations of the partial charges showed that the filling of the $3d$ band in the compound $CaCo_2$ by electrons is considerably different from pure Ca. This led to a change in the electronic configuration (EC) in Ca from $4(sp)^{1.53}d^{0.5}$ to $4(sp)^{1.23}d^{0.8}$. It was shown in a LMTO calculation[7] that, as a result of the $s-d$ electronic transition, analogous changes of the EC in pure Ca first occur at 7 GPa.

Our computed density of states $N(E)$ in $CaCo_2$ in the paramagnetic state (Fig. 3) has the typical form for compounds with C15 structure and a d transition element as the second component. It is well known that the rigid-band approximation works well for such compounds.[32] For example, the EDS differs little from that in the pseudobinary compounds $Y(Fe_{1-x}Co_x)_2$ investigated theoretically in Ref. 33. The form of the EDS shows that, on the basis of properties, $CaCo_2$ is closer to YFe_2 than YCo_2. More accurately, it is closer to compound YFeCo, whose isovalent analog it is (both possess twelve s and twenty-eight d valence electrons in the unit cell).

It follows from the data in Table I that in the compound $CaCo_2$ the number of d electrons per Co atom is essentially no greater than in pure cobalt. As a result, the calculation gives a moment per Co atom in $CaCo_2$ that is close to the moment for pure Co, in qualitative agreement with the experimental value. Ferrimagnetic ordering of sublattices with a small induced negative moment on Ca was obtained in the calculation. We note that in YFeCo the average moment per $3d$ atom is $1.62\mu_B$, and the moment per yttrium atom is $-0.42\mu_B$.[33]

The observed Curie temperature in $CaCo_2$, $T_C=528$ K, is close to the Curie temperature in YFe_2, which is 542 K.[32] This shows that the exchange interaction ion the Co sublattice is comparable to the exchange interaction in the Fe sublattice in YFe_2.

In YCo_2 there are twelve s and thirty d valence electrons per unit cell. As a result, in accordance with the rigid-band model, the Stoner criterion is not met and the ground state should be paramagnetic. This is confirmed by calculations of the electronic structure.[33,34] The calculations in Ref. 34 show that YCo_2 in an external magnetic field should transform into a ferrimagnetic state with magnetic moments $\mu_{Co}=1.02\mu_B$ and $\mu_Y=-0.28\mu_B$. This transition was later observed in an external magnetic field of the order of 100 T.[35]

The results presented suggest that for compounds of $3d$ transition metals with nonmagnetic metals with a cubic Laves phase structure (of the type YCo_2, $LaCo_2$, $LuCo_2$, YNi_2, and so on), for which good agreement is observed with the rigid-band approximation, there exists a critical density n_c of $s-d$ valence electrons. If the total number of $s-d$ valence electrons per cell is $\leqslant 40$, then the ferromagnetic (ferrimagnetic) state is stable; however, if $n\geqslant 42$, then an exchange-enhanced paramagnetic state (metamagnet) is observed.

In summary, we have observed that above 6.0 GPa a new compound $CaCo_2$ with $MgCu_2$ (C15) structure forms as a result of a pressure-induced electronic $s-d$ transition. Additional filling of the d band of Co essentially does not occur in this compound, and this results in the appearance of a stable ferromagnetic state in which a high-spin magnetic state of the Co ion is realized. The magnetic exchange interaction in the ferromagnetic $CaCo_2$ is comparable to the exchange interaction of the Fe sublattice in ferromagnetic C15 Laves phases obtained at normal pressure. It is entirely possible that at higher pressures both the compound $CaFe_2$ and a variety of pseudobinary compounds $Ca(Fe_{1-x}Co_x)_2$ with a high Curie temperature, where high-spin states of the Co and Fe ions will be realized, can form at higher pressures.

We thank S. Yu. Savrasov for providing a software package for electronic structure calculations and E. G. Maksimov for a helpful discussion of the computational results.

This work was supported by the Russian Fund for Fundamental Research (Grant No. 96-02-17541).

[1] T. Atou, M. Hasegawa, L. J. Parker, and J. V. Badding, J. Am. Chem. Soc. **118**, 12104 (1996).
[2] M. Hasegawa, T. Atou, and J. V. Badding, J. Solid State Chem. **130**, 311 (1997).
[3] L. J. Parker, M. Hasegawa, T. Atou, and J. V. Badding, Rev. High Pressure Sci. Technol. **7**, 1049 (1998).
[4] L. J. Parker, T. Atou, and J. V. Badding, Science **273**, 95 (1996).
[5] M. S. T. Bukowinski and L. Knopoff, in *High-Pressure Research: Applications in Geophysics*, edited by M. H. Manghnani and S. Akimoto, Academic Press, New York, 1977, pp. 367–387.
[6] R. Jeanloz, Annu. Rev. Earth Planet Sci. **18**, 357 (1990).

[7] H. L. Skriver, Phys. Rev. Lett. **49**, 1768 (1982).
[8] A. K. MacMahau, Physica **139–140**, 31 (1986).
[9] K. Takemura, S. Minomura, and O. Shimomura, Phys. Rev. Lett. **49**, 1772 (1982).
[10] H. Tups, K. Takemura, and K. Syassen, Phys. Rev. Lett. **49**, 1776 (1982).
[11] K. Takemura and K. Syassen, Phys. Rev. B **32**, 2213 (1985).
[12] K. Syassen, G. Wortmann, J. Feldhaus *et al.*, Phys. Rev. B **26**, 4745 (1982).
[13] J. F. Cannon, P. L. Robertson, and H. T. Hall, Mater. Res. Bull. **7**, 5 (1972).
[14] N. L. Eatough and H. T. Hall, Inorg. Chem. **11**, 2608 (1972).
[15] A. V. Tsvyashchenko and S. V. Popova, J. Less-Common Met. **90**, 211 (1983).
[16] A. V. Tsvyashchenko, J. Less-Common Met. **118**, 103 (1986).
[17] A. V. Tsvyashchenko and L. N. Fomicheva, J. Less-Common Met. **155**, 161 (1989).
[18] L. G. Khvostantsev, L. F. Vereshchagin, and A. P. Novikov, High Temp.-High Press. **9**, 637 (1977).
[19] A. R. Miedema, J. Less-Common Met. **46**, 67 (1976).
[20] O. I. Bodak and E. I. Gladyshevskiĭ, Dokl. Akad. Nauk URSR **5**, 489 (1966).
[21] V. N. Trofimov, Cryogenics **32**, 513 (1992).
[22] V. A. Sidorov and L. G. Khvostantsev, J. Magn. Magn. Mater. **129**, 356 (1994).
[23] H. P. Myers and W. Sucksmith, Proc. R. Soc. London, Ser. A **207**, 427 (1951).
[24] R. Z. Levitin and A. S. Markosyan, Usp. Fiz. Nauk **155**, 623 (1988) [Sov. Phys. Usp. **31**, 730 (1988)].
[25] E. P. Wohfarth and P. Rhodes, Philos. Mag. **7**, 1817 (1962).
[26] W. Kohn and L. J. Sham, Phys. Rev. A **140**, 1133 (1965).
[27] O. K. Andersen, Phys. Rev. B **12**, 864 (1975).
[28] E. G. Maksimov and S. Yu. Savrasov, Usp. Fiz. Nauk **165**, 773 (1995).
[29] V. L. Moruzzi, J. F. Janak, and A. R. Williams, *Calculated Electronic Properties of Metals*, Pergamon Press, New York, 1978.
[30] O. Eriksson, M. S. S. Brooks, and B. Johansson, Phys. Rev. B **39**, 13115 (1989).
[31] S. N. Vaidya and G. C. Kennedy, Phys. Chem. Solids **31**, 2329 (1970).
[32] K. H. J. Buschow, Rep. Prog. Phys. **40**, 1179 (1977).
[33] O. Eriksson, B. Johansson, M. S. S. Brooks, and H. L. Skriver, Phys. Rev. B **40**, 9519 (1989).
[34] K. Schwarz and P. Mohn, J. Phys. F **14**, L129 (1984).
[35] T. Goto, K. Fukamichi, T. Sakakibara, and H. Komatsu, Solid State Commun. **72**, 945 (1989).

Translated by M. E. Alferieff

Orbital magnetism in small quantum dots with closed shells

W. D. Heiss
Centre for Nonlinear Studies and Department of Physics, University of the Witwatersrand, Johannesburg, South Africa

R. G. Nazmitdinov
Centre for Nonlinear Studies and Department of Physics, University of the Witwatersrand, Johannesburg, South Africa;
Joint Institute for Nuclear Research, 141980 Dubna, Russia

(Submitted 10 November 1998)
Pis'ma Zh. Éksp. Teor. Fiz. **68**, No. 12, 870–875 (25 December 1998)

It is found that various kinds of shell structure which occur at specific values of the magnetic field lead to the disappearance of the orbital magnetization for particular magic numbers in small quantum dots with electron number $A<30$. © *1998 American Institute of Physics.* [S0021-3640(98)00424-1]

PACS numbers: 73.20.Dx, 73.61.−r

The development of semiconductor technology has made possible the confinement of a finite number of electrons in a localized space of a few hundred angstroms.[1] These mesoscopic systems called quantum dots open up new avenues in the study of the interplay between quantum and classical behavior at a low-dimensional scale. The smaller the quantum dot, the larger the prevalence of quantum effects upon the static and dynamic properties of the system. Their electronic properties are determined by the interplay of the external confinement and the electron–electron interaction, which produces the effective mean field of the ''artificial atom.''[2,3]

The quasiparticle concept associated with an effective mean field is well established in many-particle physics. For finite Fermi systems like nuclei or metallic clusters the bunching of single-particle levels known as shells[4,5] is one consequence of this description, if the mean free path of the particles is comparable with the size of the system. A remarkable stability is found in nuclei and metallic clusters at magic numbers, which correspond to closed shells in the effective potential. For small quantum dots, where the number of electrons is well defined ($A<30$), the mean free path of the electrons appears to be comparable with the diameter of the dot. Transport phenomena are governed by the physics of the Coulomb blockade regime.[3] In recent experiments[6–8] shell structure effects have been observed clearly for quantum dots. In particular, the energy needed to place the extra electron (addition energy) into a vertical quantum dot at zero magnetic field has characteristic maxima which correspond to the sequence of magic numbers of a two-dimensional harmonic oscillator.[7] The energy gap between filled shells is $\hbar\omega_0$, where $\hbar\omega_0$ is the lateral confinement energy. In fact, for the case when the confining energy is

comparable to or larger than the interaction energy, these atomic-like features have been predicted in a number of publications.[9–12] While the electron–electron interaction is important for the explanation of certain ground-state properties such as special values of the angular momenta of quantum dots in a magnetic field,[2] for small number of electrons the confinement energy becomes prevalent over the Coulomb energy.[9,12,13] In Ref. 14 it was demonstrated that the magnetoexciton spectrum in small quantum dots resembles well the spectrum of noninteracting electron–hole pairs. In particular, the gaps in the spectrum, which are typical features of the shell structure, reappear at different values of the magnetic field. Recent calculations using the spin-density-functional approach[15] nicely confirm shell closure for small magic electron numbers in a parabolic quantum dot.

Orbital magnetism of an ensemble of quantum dots was discussed for noninteracting electrons in Refs. 16–18, but little attention was paid to the shell structure of an individual dot. We demonstrate within a simple model that the disappearance and reappearance of closed shells in a quantum dot under variation of the magnetic field strength leads to a novel feature: the orbital magnetization disappears for particular values of the magnetic field strength, which are associated to particular magic numbers.

Since the electron interaction is crucial only for partially filled electronic shells,[15,19] we deal in this paper mainly with closed shells. This case corresponds to the quantum limit $\hbar\omega_0 \geqslant e^2/\varepsilon l_0$, where $e^2/\varepsilon l_0$ is the typical Coulomb energy ($l_0=(\hbar/m^*\omega_0)^{1/2}$, m^* is the effective electron mass, and ε is the dielectric constant). In fact, for small dots, where large gaps between closed shells occur,[9,12,14] the electron interaction plays the role of a weak perturbation which can be neglected. But even in the regime $\hbar\omega_0 < e^2/\varepsilon l_0$ a distinctively larger addition energy is needed, if an electron is added to a closed shell.[15] We choose the harmonic oscillator potential as the effective mean field for the electrons in an isolated quantum dot. Our discussion here is based upon the 2D version of the Hamiltonian[20] including the spin degree of freedom. The magnetic field is perpendicular to the plane of motion, i.e., $H=\Sigma_{j=1}^{A} h_j$ with

$$h=\frac{1}{2m^*}\left(\mathbf{p}-\frac{e}{c}\mathbf{A}\right)^2+\frac{m^*}{2}(\omega_x^2x^2+\omega_y^2y^2)+\mu^*\sigma_z B, \tag{1}$$

where $\mathbf{A}=(\mathbf{r}\times\mathbf{B})/2, \mathbf{B}=(0,0,B)$, and σ_z is the Pauli matrix. We do not take into account the effect of finite temperature; this is appropriate for experiments which are performed at temperatures $kT \ll \Delta$, where Δ is the mean level spacing. The units used are meV for the energy and tesla for the magnetic field strength. The effective mass is $m^*=0.067m_e$ for GaAs, which yields, for $A\approx 15$, the size $R_0\approx 320$ Å and $\hbar\omega_0=3$ meV.[20] The effective mass determines the orbital magnetic moment for the electrons and leads to $\mu_B^{\mathrm{eff}}=m_e/m^*\mu_B\approx 15\mu_B$. The effective spin magnetic moment is $\mu^*=g_L\mu_B$, with the effective Landé factor $g_L=0.44$ and $\mu_B=|e|\hbar/2m_ec$. The magnetic orbital effect is much enhanced in comparison with the magnetic spin effect, yet the tiny spin splitting does produce signatures as we see below.

Shell structure occurs whenever the ratio of the two eigenmodes $\Omega_\pm$ of the Hamiltonian (1) (see Ref. 20),

$$\Omega_\pm^2=\frac{1}{2}(\omega_x^2+\omega_y^2+4\omega_L^2\pm\sqrt{(\omega_x^2-\omega_y^2)^2+8\omega_L^2(\omega_x^2+\omega_y^2)+16\omega_L^4}), \tag{2}$$

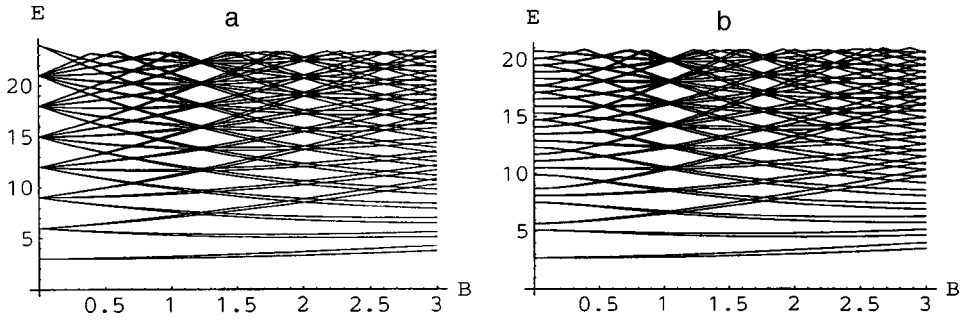

FIG. 1. Single-particle spectra as a function of the magnetic field strength. Spectra are displayed for (a) a plane isotropic and (b) a deformed two-dimensional oscillator.

is a rational number with a small numerator and denominator. Here $\omega_L=|e|B/(2m^*c)$. Closed shells are particularly pronounced if the ratio is equal to one (for $B=0$) or two (for $B\approx 1.23$) or three (for $B\approx 2.01$) and less pronounced if the ratio is 3/2 (for $B=0.72$) or 5/2 (for $B=1.65$) for the circular case $\omega_x=\omega_y$ (see Fig. 1a). Note that, for better illustration, we used for the spin splitting the value $2\mu_B$ instead of the correct μ^* in all figures; the discussions and conclusions are based on the correct value. The values given here for B depend on m^* and $\omega_{x,y}$. As a consequence, a material with an even smaller effective mass m^* would show these effects at a correspondingly smaller magnetic field. For $B=0$ the magic numbers (including spin) turn out to be the usual sequence of the two-dimensional isotropic oscillator, that is 2, 6, 12, 20, . . . (Ref. 7). For $B\approx 1.23$ we find new shells as if the confining potential were be a deformed harmonic oscillator without a magnetic field. The magic numbers are 2, 4, 8, 12, 18, 24, . . . , which are just the numbers obtained from the two-dimensional oscillator with $\omega_>=2\omega_<$ ($\omega_>$ and $\omega_<$ denote the larger and smaller value of the two frequencies). Similarly, for $B\approx 2.01$ we get the sequence of magic numbers 2, 4, 6, 10, 14, 18, 24, . . . , which corresponds to $\omega_>=3\omega_<$. If we start from the outset with a deformed mean field $\omega_x=(1-\beta)\omega_y$ with $\beta>0$, the degeneracies (closed shells) lifted at $B=0$ reoccur at higher values of B (see Fig. 2 and the discussion relating to it). In Fig. 1b we display an example for $\beta=0.2$. The significance of this finding lies in the fact that closed shells are restored by a magnetic field in an isolated quantum dot which does not have magic numbers due to deformation at zero field. We mention that the choice $\beta=0.5$ would shift the pattern found at $B\approx 1.23$ in Fig. 1a to the value $B=0$. The relation between B and the deformation is displayed in Fig. 2, where, for better illustration, $B'=\omega_L/\omega_x$ rather than B is plotted versus $r=\omega_x/\omega_y$. Closed shells are obtained for values of B and β which yield $\Omega_+/\Omega_-=k=1,2,3,\ldots$, that is, for values on the trajectories of Fig. 2.

Note also the asymmetry of the curves in Fig. 2: although $\omega_x/\omega_y=r$ is physically identical with $\omega_x/\omega_y=1/r$ in zero magnetic field, the two deformations become distinct in the presence of a magnetic field, as it establishes a direction perpendicular to the $x-y$ plane.

In Ref. 20 we obtained various shapes of the quantum dot by energy minimization. In this context it is worth noting that at the particular values of the magnetic field for which a closed shell occurs, the energy minimum will be obtained for circular dots if the particle number is chosen equal to a magic number. Deviations from magic numbers

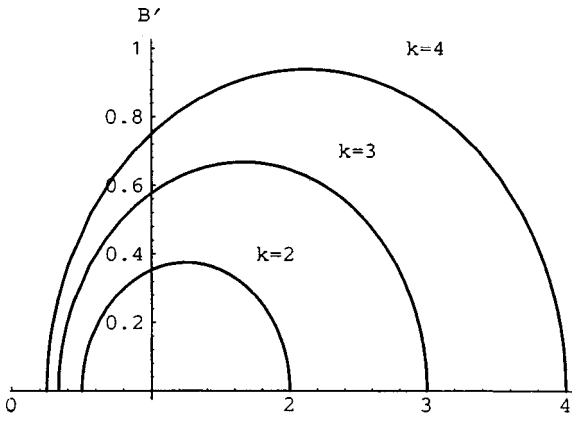

FIG. 2. Relative magnetic field strength $B'=\omega_L/\omega_x$ as a function of the ratio $r=\omega_x/\omega_y=1-\beta$ for fixed values of the ratio $k=\Omega_+/\Omega_-$.

usually give rise to deformed shapes at the energy minimum. To what extent these ''spontaneous'' deformations (the Jahn–Teller effect)[21]) actually occur must be ascertained from more-detailed experimental information. Far-infrared spectroscopy in a small isolated quantum dot could be a useful tool to provide pertinent data.[20]

The question arises as to what extent our findings depend upon the particular choice of the mean field. The Coulomb interaction lowers the electron levels for increasing magnetic quantum number $|m|$ (Refs. 2, 13). The addition of the term $-\lambda\hbar\omega L^2$ to the Hamiltonian (1), where L is the dimensionless z component of the angular momentum operator, mimics this effect for $\lambda>0$ in the Coulomb blockade regime of deformed quantum dots.[22] In this way, it interpolates the single-particle spectrum between that of the oscillator and that of the square well.[4] For $\omega_x\neq\omega_y$ and $\lambda\neq 0$ the Hamiltonian $H'=H-\lambda\hbar\omega L^2$ is nonintegrable,[23] and the level crossings encountered in Fig. 1 become avoided level crossings. The shell structure, which prevails for $\lambda=0$ throughout the spectrum at $B\approx 1.23$ or $B\approx 2.01$, is therefore disturbed to an increasing extent with increasing shell number. But even for $\lambda\leqslant 0.1$ the structure is still clearly discernible for about seven shells, that is, for particle numbers up to about twenty five.

When the magnetic field is changed continuously for a quantum dot of fixed electron number, the ground state will undergo a rearrangement at the values of B where level crossings occur.[2,13] In fact, it leads to strong variations in the magnetization[2] and should be observable also in the magnetic susceptibility, as it is proportional to the second derivative of the total energy with respect to the field strength. While details may be modified by electron correlations, we think that the general features discussed below should be preserved.

In Fig. 3 we discern clearly distinct patterns depending on the electron number; in fact, the susceptibility turns out to be a ''fingerprint'' for the electron number. Deforming the oscillator does not produce new features except for the fact that all lines in Fig. 3 will be shifted in accordance with Fig. 2. If there is no level crossing, the second derivative of $E_{\rm tot}$ is a smooth function. The crossing of two occupied levels does not change the smoothness. In contrast, if an unoccupied level crosses the last occupied level, the second

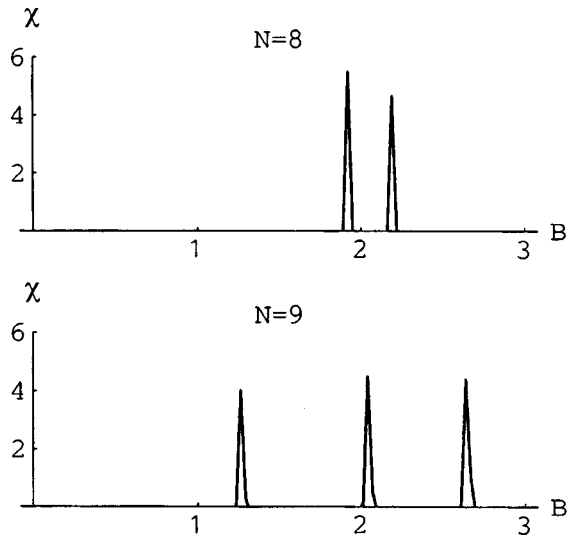

FIG. 3. Magnetic susceptibility $\chi=-\partial^2 E_{\rm tot}/\partial B^2$ in arbitrary units as a function of the magnetic field strength for the isotropic oscillator without the L^2 term. $E_{\rm tot}$ is the sum of the single-particle energies filled from the bottom up to electron number A.

derivative of $E_{\rm tot}$ must show a spike. In this way, we understand the even–odd effect when comparing $A=8$ with $A=9$ in Fig. 3. The spin splitting caused by the magnetic field at $B\approx 2.01$ for $A=8$ is absent for $A=9$. This becomes evident when looking at a blowup of this particular level crossing, which is illustrated in Fig. 4, where the last occupied level is indicated as a thick line and the points where a spike occurs are indicated by a dot. Note that the splitting is proportional to the effective spin magnetic moment μ^*.

Spikes of the susceptibility are associated with a spin flip for even electron numbers. They are brought about by the crossing of the top (bottom) line with the bottom (top) line of a double line. Hence, both lines of the double splitting in Fig. 3 yield a spin flip ($A=8$), but neither of the single lines does ($A=9$). Strictly speaking, the spikes are δ functions with a factor which is determined by the angle at which the two relevant lines cross. If the level crossings are replaced by avoided crossings (Landau–Zener crossings), the lines will be broadened. This would be the case in the present model for $\lambda>0$ and $\beta>0$. Finite temperature will also result in line broadening.

We now focus on the special cases which give rise to closed shells, that is when the ratio $\Omega_+/\Omega_-=k=1,2,3,\ldots$. For the sake of clarity we analyze in detail the circular

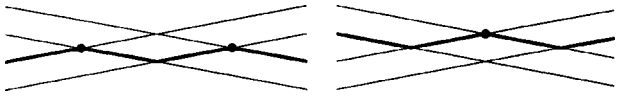

FIG. 4. Blowups of the relevant level crossings explaining the features in Fig. 3. The left- and right-hand sides are for $A=8$ and $A=9$, respectively.

shape ($\omega_x=\omega_y=\omega_0$) for which the eigenmodes (Eq. (2)) become $\Omega_\pm=(\Omega\pm\omega_L)$ with $\Omega=\sqrt{\omega_0^2+\omega_L^2}$ (Ref. 24). We find for the magnetization

$$M=\mu_B^{\rm eff}\left(1-\frac{\omega_L}{\Omega}\right)\left(\sum\nolimits_- -k\sum\nolimits_+\right)-\mu^*\langle S_z\rangle\,, \tag{3}$$

with $\Sigma_\pm=\Sigma_j^A(n_\pm+1/2)_j$ (Ref. 20). For a completely filled shell $\langle S_z\rangle=0$, since, for the magnetic field strengths considered here, the spin orientations cancel each other (see Fig. 1). From the orbital motion we obtain for the susceptibility

$$\chi=dM/dB=-\frac{\mu_B^{\rm eff^2}}{\hbar\Omega}\left(\frac{\omega_0}{\Omega}\right)^2\left(\sum\nolimits_+ +\sum\nolimits_-\right). \tag{4}$$

It follows from Eq. (4) that for a completely filled shell, the magnetization owing to the orbital motion leads to diamagnetic behavior. For zero magnetic field ($k=1$) the system is paramagnetic, and the magnetization vanishes ($\Sigma_-=\Sigma_+$). The value $k=2$ is attained at $B\approx 1.23$. When calculating Σ_- and Σ_+ we have to distinguish between the cases where the shell number N of the last filled shell is even or odd. With all shells filled from the bottom we find (i) if the last filled shell number is even:

$$\sum\nolimits_+=\frac{1}{12}(N+2)[(N+2)^2+2],\quad \sum\nolimits_-=\frac{1}{6}(N+1)(N+2)(N+3),$$

which implies

$$M=-\mu_B^{\rm eff}(1-\omega_L/\Omega)(N+2)/2;$$

and (ii) if the last filled shell number is odd:

$$\sum\nolimits_+=\frac{1}{2}\sum\nolimits_-=\frac{1}{12}(N+1)(N+2)(N+3)$$

which, in turn, implies $M=0$. Therefore, if $\Omega_+/\Omega_-=2$, the orbital magnetization vanishes for the magic numbers 4, 12, 24, . . . , while it leads to diamagnetism for the magic numbers 2, 8, 18, ... A similar picture is obtained for $\Omega_+/\Omega_-=3$ which happens at $B\approx 2.01$: for each third filled shell number (magic numbers 6,18, . . .) the magnetization is zero. Since the results presented are due to shell effects, they do not depend on the assumption $\omega_x/\omega_y=1$ which was made to facilitate the discussion. The crucial point is the relation $\Omega_+/\Omega_-=k=1,2,3,\ldots$, which can be obtained for a variety of combinations of magnetic field strength and the ratio ω_x/ω_y, as is illustrated in Fig. 2. Whenever the appropriate combination of field strength and deformation is chosen to yield, say, $k=2$, our findings apply.

To summarize: the consequences of shell structure effects for the addition energy of a small isolated quantum dot have been analyzed. At certain values of the magnetic field strength, closed shells appear in a quantum dot even in cases where deformation does not give rise to magic numbers at zero field. Measurements of the magnetic susceptibility are expected to reflect the properties of the single-particle spectrum and should display characteristic patterns depending on the particle number. At certain values of the magnetic field and electron numbers the orbital magnetization vanishes due to shell closure in the quantum dot.

[1] M. A. Kastner, Phys. Today **46**, 24 (1993); R. C. Ashoori, Nature (London) **379**, 413 (1996).
[2] P. A. Maksym and T. Chakraborty, Phys. Rev. Lett. **65**, 108 (1990); Phys. Rev. B **45**, 1947 (1992); M. Wagner, U. Merkt, and A. V. Chaplik, Phys. Rev. B **45**, 1951 (1992); P. Hawrylak, Phys. Rev. Lett. **71**, 3347 (1993).
[3] L. P. Kouwenhoven *et al.*, *Mesoscopic Electron Transport*, Proceedings of the NATO ASI, edited by L. P. Kouwenhoven, G. Schön, and L. L. Sohn (Series **E345**), Kluwer, Dordrecht, Netherlands, 1997, p. 105.
[4] S. G. Nilsson and I. Ragnarsson, *Shapes and Shells in Nuclear Structure*, Cambridge, Cambridge University Press 1995.
[5] W. A. de Heer, Rev. Mod. Phys. **65**, 611 (1993); M. Brack, Rev. Mod. Phys. **65**, 677 (1993).
[6] D. J. Lockwood, P. Hawrylak, P. D. Wang *et al.*, Phys. Rev. Lett. **77**, 354 (1996).
[7] S. Tarucha, D. G. Austing, T. Honda *et al.*, Phys. Rev. Lett. **77**, 3613 (1996).
[8] M. Fricke *et al.*, Europhys. Lett. **36**, 197 (1996).
[9] M. Macucci, K. Hess, and G. J. Iafrate, Phys. Rev. B **48**, 17354 (1993); J. Appl. Phys. **77**, 3267 (1995).
[10] P. A. Maksym, Phys. Rev. B **53**, 10871 (1996).
[11] W. D. Heiss and R. G. Nazmitdinov, Phys. Lett. A **222**, 309 (1996).
[12] M. Stopa, Phys. Rev. B **54**, 13767 (1996).
[13] M. Dineykhan and R. G. Nazmitdinov, Phys. Rev. B **55**, 13707 (1997).
[14] A. Wojs, P. Hawrylak, S. Fafard, and L. Jacak, Phys. Rev. B **54**, 5604 (1996).
[15] K. Hirose and N. S. Wingreen, http://xxx.lanl.gov/abs/cond-mat/9808193.
[16] B. L. Altshuler, Y. Gefen, and Y. Imry, Phys. Rev. Lett. **66**, 88 (1991); B. L. Altshuler *et al.*, Phys. Rev. B **47**, 10335 (1993).
[17] F. V. Oppen, Phys. Rev. B **50**, 17151 (1994).
[18] K. Richter, D. Ulmo, and R. Jalabert, Phys. Rep. **276**, 1 (1996).
[19] A. Wojs and P. Hawrylak, Phys. Rev. B **53**, 10841 (1996); M. Eto, Jpn. J. Appl. Phys., Part 1 **36**, 3924 (1997); M. Koskinen, M. Manninen, and S. M. Reimann, Phys. Rev. Lett. **79**, 1389 (1997).
[20] W. D. Heiss and R. G. Nazmitdinov, Phys. Rev. B **55**, 16310 (1997).
[21] H. A. Jahn and E. Teller, Proc. R. Soc. London, Ser. A **161**, 220 (1937).
[22] G. Hackenbroich, W. D. Heiss, and H. A. Weidenmüller, Phys. Rev. Lett. **79**, 127 (1997).
[23] W. D. Heiss and R. G. Nazmitdinov, Phys. Rev. Lett. **73**, 1235 (1994); Physica D **118**, 134 (1998).
[24] V. Fock, Z. Phys. **47**, 446 (1928).

Published in English in the original Russian journal. Edited by Steve Torstveit.

Surface polaritons in a dielectric at a boundary with a metal in a static electric field

I. E. Chupis and D. A. Mamaluĭ*

B. I. Verkin Physicotechnical Institute of Low Temperatures, Ukrainian National Academy of Sciences, 310164 Kharkov, Ukraine

(Submitted 12 November 1998)
Pis'ma Zh. Éksp. Teor. Fiz. **68**, No. 12, 876–880 (25 December 1998)

The existence of surface polaritons in a dielectric at a boundary with an ideal metal or superconductor in a static electric field is predicted. The frequency regions in which polaritons exist are substantially different for opposite orientations of the electric field, so that a change in the direction of the field signifies ''switching on'' or ''switching off'' of surface polaritons with a fixed frequency. © *1998 American Institute of Physics.* [S0021-3640(98)00524-6]

PACS numbers: 71.36.+c, 77.84.−s

The present letter examines the effect of a static electric field, external or spontaneous (if the dielectric is a ferroelectric), on surface polariton excitations in a bulk dielectric crystal at a boundary with a metal. It is well known that when a bulk dielectric is in contact with a metal, surface polaritons in the dielectric cannot exist.[1] It will be shown below that a static electric field lifts this prohibition, and surface polariton waves, whose penetration depth is inversely proportional to the static electric field, arise in the dielectric. In Ref. 2 it was reported that an electromagnetic wave in the presence of a static electric field induces an off-diagonal component of the high-frequency magnetoelectric (ME) susceptibility. It will be shown below that this ME interaction is responsible for the appearance of surface polaritons in a dielectric at its boundary with a metal.

The effect of the spontaneous ME susceptibility on surface polaritons in magnets with a linear magnetoelectric effect has been studied in a number of works (see, for example, the latest work in Ref. 3). The ME interaction was described by a potential ME energy whose form depends on the symmetry of the crystal. The effect of a *dynamic* ME interaction on surface polaritons in a ferroelectric was studied in Ref. 4. This ME interaction energy is a scalar, and therefore it is present in a crystal with any symmetry. Besides this, its existence does not require the presence of any spontaneous ordering. The effect of this ME energy on surface polariton waves is investigated below.

Let us consider a dielectric occupying the half space $z>0$ and bordering a metal ($z<0$), in the presence of a static electric field $\mathbf{E}_0$ oriented in a direction normal to the surface (z axis). For definiteness, we assume the dielectric to be uniaxial (z is the easy axis), though the results obtained below are general.

The energy density W of the dielectric consists of an electric-dipole term W_e and the interaction energy W_{int} with external fields, $W=W_e+W_{\text{int}}$, where

$$W_e=\frac{C_1}{2}P_z^2+\frac{C_2}{2}(P_x^2+P_y^2)+\frac{\Pi^2}{2\rho},$$

$$W_{\text{int}}=-\mathbf{P}\cdot\mathbf{E}+\xi\mathbf{P}\cdot(\mathbf{\Pi}\times\mathbf{h}). \quad (1)$$

Here $\mathbf{E}=\mathbf{E}_0+\mathbf{e}$, and $\mathbf{e}$ and $\mathbf{h}$ are the alternating electric and magnetic fields. The last term in W_e is the kinetic energy density, and $\mathbf{\Pi}$ is the momentum density. The term with the coefficient ξ in W_{int} is the above-mentioned scalar ME energy of dynamic origin. This is the interaction energy of the electric polarization $\mathbf{P}$ with the effective electric field $\mathbf{E}_{\text{eff}}=c^{-1}(\mathbf{V}\times\mathbf{h})$ produced by the motion of a charge with velocity $\mathbf{V}$ in a magnetic field $\mathbf{h}$. Since $\mathbf{\Pi}=(m/v_0)\mathbf{V}$, the constants have the values $\xi=v_0/mc$ and $\rho=m/v_0$, where m is the mass of the charged particle, v_0 is the unit cell volume, and c is the speed of light. Generally speaking, the polarization $\mathbf{P}$ contains both ionic and electronic contributions. In the infrared region of the spectrum, especially near the characteristic ionic frequencies, the ionic polarizability prevails, the ions make the largest contribution to the dynamic ME energy, and therefore m and $\mathbf{\Pi}$ are, respectively, the ion mass and momentum. In the optical region of the spectrum, however, where the electronic polarizability is much greater than the ionic polarizability, m is the electron mass and $\mathbf{\Pi}$ is the electron momentum.

If the dielectric is not a ferroelectric, then $C_1>0$ and the equilibrium electrical polarization P_{0z} in a static electric field $\mathbf{E}_0$ directed along the easy axis is, as follows from Eq. (1), $P_{0z}=E_{0z}/C_1$. For a ferroelectric the constant $C_1<0$, the energy W_e should include an anharmonic term $\delta P_z^4/4$, and the spontaneous polarization vector is $P_{0z}=\pm(-C_1/\delta)^{1/2}$. If the dielectric is a ferroelectric, we assume that there is no static electric field.

The linear response of a nonmagnetic dielectric with magnetic permeability $\mu=1$ to the field of an electromagnetic wave in the absence of damping and in neglect of spatial dispersion is described by the following electric (χ_{ik}^e) and magnetic ($\chi_{ik}^{em}=\partial P_i/\partial h_k=(\chi_{ki}^{em})^*$) susceptibilities:[2]

$$\chi_{xx}^e=\chi_{yy}^e=\bar{\omega}_0^2/(\omega_0^2-\omega^2), \quad \chi_{zz}^e=\bar{\omega}_0^2/(\omega_e^2-\omega^2),$$

$$\chi_{xy}^{em}=-i\gamma/4\pi, \quad \gamma=4\pi\omega g P_{0z}/(\omega_0^2-\omega^2), \quad (2)$$

where

$$\omega_0=\bar{\omega}_0\sqrt{C_2}, \quad \omega_e=\bar{\omega}_0\sqrt{C_1},$$

$$\bar{\omega}_0^2=e^2/mv_0, \quad g=e\xi/v_0=e/mc. \quad (3)$$

Here ω_0 is the frequency of excitations of the transverse polarization components P_x and P_y, and ω_e is the frequency of excitations of P_z in the direction of the easy axis z. For a ferroelectric $\omega_e=\bar{\omega}_0\sqrt{-2C_1}$ is the ferroelectric soft mode. For a uniaxial dielectric, which are considering, $\omega_0>\omega_e$.

The relation between the electric $\mathbf{d}$ and magnetic $\mathbf{b}$ inductions with field intensities $\mathbf{e}$ and $\mathbf{h}$ in the presence of ME susceptibility is given by the equations

$$d_i=\varepsilon_{ik}e_k+4\pi\chi_{ik}^{em}h_k, \quad b_i=\mu_{ik}h_k+4\pi\chi_{ik}^{me}e_k,$$

$$\varepsilon_{ik}=\varepsilon^{*}_{ki}=\delta_{ik}+4\pi\chi^{e}_{ik}, \quad \mu_{ik}=\mu^{*}_{ki}, \quad \chi^{em}_{ik}=(\chi^{me}_{ki})^{*}. \tag{4}$$

In our case the nonzero off-diagonal component of the ME susceptibility $\chi^{em}_{xy}=\partial P_x/\partial h_y \propto E_{0z}$, i.e., in the presence of a static electric field E_{0z} the magnetic field h_y of the electromagnetic wave induces an ac component of the electric polarization p_x (high-frequency analog of the Hall effect). Since the excitation $p_x \propto \Pi_x$, in other words, an ac toroidal moment $\Pi_x \propto E_{0z}h_y$ is induced in the dielectric.

We seek a solution of Maxwell's equations for waves propagating along the interface with a metal in the direction of the x axis ($k=k_x$) in the form

$$\mathbf{e}, \mathbf{h} \propto e^{i(kx-\omega t)-k_0 z}, \tag{5}$$

where $k_0>0$ is the inverse penetration depth of the surface excitations in the dielectric.

The conditions

$$b_z=\tilde{b}_z, \quad \mathbf{h}_t=\tilde{\mathbf{h}}_t, \quad d_z=\tilde{d}_z, \quad \mathbf{e}_t=0 \tag{6}$$

should hold at the interface with an ideally conducting metal. In Eq. (6) the symbols with the tildes denote quantities referring to the metal; the index t refers to the tangential components of the fields. For a superconductor $b_z=0$ in Eq. (6).

It is easy to see that, taking account of Eqs. (4) and (2) and the boundary conditions (6), Maxwell's equations in a dielectric describe excitations for which $e_x=e_y=h_x=h_z=0$ and e_z and h_y satisfy the equations

$$\left(k_0+\frac{\omega}{c}\gamma\right)h_y=0, \quad ke_z+\frac{\omega}{c}h_y=0, \quad \frac{\omega}{c}\varepsilon e_z+kh_y=0, \tag{7}$$

where

$$\varepsilon=\varepsilon_{zz}=\frac{\Omega_e^2-\omega^2}{\omega_e^2-\omega^2}, \quad \Omega_e^2=\omega_e^2+4\pi\overline{\omega_0^2}. \tag{8}$$

In our case $b_z=h_z=0$, and therefore the results obtained below also hold for a dielectric in contact with a superconductor. It is evident from the first equation in Eq. (7) that in the absence of a ME interaction ($\gamma=0$, $E_{0z}=0$) there exists a wave only with $k_0=0$, i.e., surface polaritons are absent, polariton excitations are volume excitations (their penetration depth $k_0^{-1}=\infty$). In the presence of an electric field E_{0z} ($\gamma\neq 0$), however, the prohibition on the existence of surface polaritons is lifted. There are no volume polaritons in the dielectric; the polaritons become surface polaritons. The penetration depth of polaritons in the dielectric is determined only by the ME interaction

$$k_0^{-1}=-\frac{c}{\omega\gamma(\omega)}, \tag{9}$$

and the dispersion relation has the same form as for volume polaritons in the case of no electric field:

$$k^2=\frac{\omega^2}{c^2}\varepsilon(\omega). \tag{10}$$

The condition

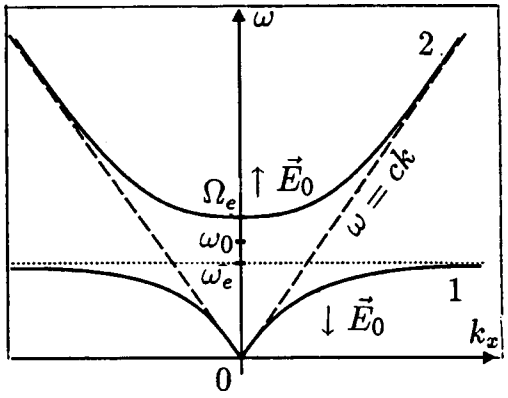

FIG. 1. Dispersion relations for optical polaritons in a dielectric for opposite directions of the electric field: curve *1* — $\mathbf{E}_0$ directed into the dielectric; *2* — $\mathbf{E}_0$ directed along the outer normal to the dielectric.

$$\gamma(\omega)<0, \quad \varepsilon(\omega)>0 \tag{11}$$

follows from Eqs. (9) and (10) and the positivity of k_0. The polariton dispersion relations (10) with the conditions (11) taken into account are presented in Fig. 1. This figure corresponds to optical excitation frequencies for which $\omega_0^2 \propto \bar{\omega}_0^2 = e^2/mv_0$, where m is the electron mass. The gyromagnetic ratio $g<0$. For $v_0 \sim 10^{-22}$ cm^3, the frequency $\omega_0 \sim 10^{15}$ rad/s. For our case of a uniaxial dielectric the condition $\Omega_e > \omega_0$ is natural, i.e., $\chi_{zz}^{-1}(0)+4\pi > \chi_{xx}^{-1}(0)$, where $\chi(0)$ is the static electric susceptibility. As one can see from Fig. 1, the surface polaritons are real.

The frequencies of surface polariton excitations are different for opposite orientations of the electric field. In a field oriented into the dielectric, the lower branch is excited, while in a field with the opposite orientation the upper branch is excited. The situation is reversed for ionic excitations ($g>0$). Thus surface polaritons with a fixed frequency can be ''switched on and off'' by changing the direction of the static electric field.

For a ferroelectric, the spontaneous polarization P_{0z} plays the role of a static electric field, and a reversal of the direction of the spontaneous polarization in 180-degree domains corresponds to a change in the direction of the field. The ''domain influence'' on surface polaritons was noted in Ref. 4. In contrast to the results obtained in Ref. 4, in the present work the difference between polariton frequencies in 180-degree domains (or when the direction of the electric field changes) is not small. This is explained by the fact that the dispersion relation (10) does not contain the small ME interaction; only the penetration depth (9) of waves in the dielectric depend on it (and is completely determined by it). We note that this penetration depth is inversely proportional to the *first* power of the coefficient γ of the small ME interaction, in contrast to surface acoustic waves in piezomagnets, studied in Ref. 5, where the penetration depth was inversely proportional to the product of small quantities — the squared magnetoelectric coefficient and the squared piezomagnetic coefficient.

In our case the penetration depth is inversely proportional to the first power of the static electric field, and the penetration depth is smaller at higher electric fields, i.e., a

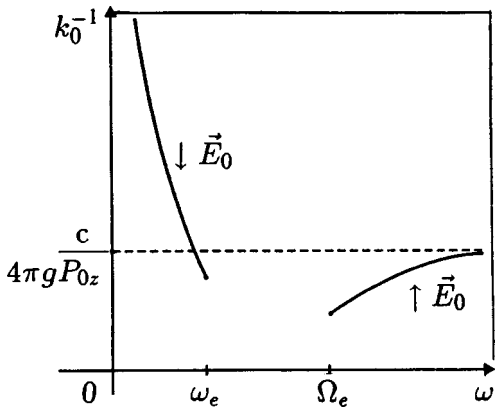

FIG. 2. Penetration depths of surface polaritons in a dielectric as a function of frequency for opposite directions of the electric field.

static electric field ''expels'' an electromagnetic field from the dielectric.

Figure 2 displays the frequency dependence of the penetration depth k_0^{-1} of polaritons in a dielectric. At optical frequencies k_0^{-1} is of the order of $c(4\pi g P_{0z})^{-1}$, which for $P_0 \sim 10^4$ cgs esu is $k_0^{-1} \sim 10^{-2}$ cm.

Let us see what happens to polariton excitations when the static electric field is switched off. As an example, let the electric field be directed along the outer normal to the dielectric. Then the branches *2* in Fig. 1 correspond to surface polariton excitations with $k_0 > 0$, and the branches *1* are ''nonphysical'' excitations with $k_0 < 1$, growing exponentially into the dielectric. As E_0 (i.e., k_0) decreases, the amplitude of the excitations corresponding to the branch *1* decreases, and when $E_0 = 0$ they become volume excitations. The excitations on the branch *2* also become volume excitations in this case, i.e., for $E_0 = 0$ the surface waves become volume waves, corresponding to the two frequency branches of the excitations — *1* and *2*. For the opposite orientation of the static electric field, the branches 1 correspond to surface polaritons and the branches 2 are ''nonphysical'' ($k_0 < 0$), which as in the preceding case become volume excitations for $k_0 = 0$, i.e., for $E_0 = 0$.

In summary, surface polaritons, which arise as a result of the ME interaction, are possible in a bulk dielectric in the plane of contact with an ideal metal or superconductor in the presence of a static electric field. The frequencies at which surface polaritons exist are substantially different for opposite orientations of the static electric field (or in 180-degree domains of a ferroelectric). This means that the frequency range of surface polaritons can be changed by switching the direction of the static electric field applied to the dielectric.

We note that an electric field does not, of course, destroy the optical reciprocity of the polariton frequency branches, $\omega(-\mathbf{k}) = \omega(\mathbf{k})$. However, it turns out that a static magnetic field also makes it possible for surface polariton excitations to exist in a dielectric at a boundary with a metal. These excitations are characterized by a strong optical nonreciprocity, $\omega(-\mathbf{k}) \neq \omega(\mathbf{k})$. These results will be the subject of a separate report.

We thank V. I. Fomin and V. S. Kurnosov for helpful discussions.

*e-mail: mamaluy@ilt.kharkov.ua

[1] V. M. Agranovich and D. L. Mills (Eds.), *Surface Polaritons*, North-Holland, Amsterdam, 1982 [Russian original, Nauka, Moscow, 1985].
[2] I. E. Chupis, Fiz. Nizk. Temp. **23**, 290 (1997) [Low Temp. Phys. **23**, 213 (1997)].
[3] V. D. Buchel'nikov and V. G. Shavrov, Zh. Éksp. Teor. Fiz. **109**, 706 (1996) [JETP **82**, 380 (1996)].
[4] I. E. Chupis and D. A. Mamaluĭ, Fiz. Nizk. Temp. **24**, 1010 (1998) [Low Temp. Phys. **24**, 762 (1998)].
[5] V. I. Al'shits and V. N. Lyubimov, Zh. Éksp. Teor. Fiz. **106**, 663 (1994) [JETP **79**, 364 (1994)].

Translated by M. E. Alferieff

Pressure-induced dimerization of C_{60} fullerene

V. A. Davydov,* L. S. Kashevarova, and A. V. Rakhmanina
L. F. Vereshchagin Institute of High-Pressure Physics, Russian Academy of Sciences, 142092, Troitsk, Moscow Region, Russia

V. M. Senyavin
M. V. Lomonosov Moscow State University, 103064 Moscow, Russia

V. Agafonov and R. Ceolin
Laboratoire de Chimie Physique, JE 408, Faculte de Farmacie, 37200 Tours, France

H. Szwarc
Laboratoire de Chimie Physique des Materiaux Amorphes, Universite Paris Sud, 91405 Orsay, France

(Submitted 27 October 1998; resubmitted 17 November 1998)
Pis'ma Zh. Éksp. Teor. Fiz. **68**, No. 12, 881–886 (25 December 1998)

The dimerization of C_{60} fullerene under conditions of quasi-hydrostatic compression at temperatures above 293 K is investigated by IR spectroscopy, Raman scattering (RS) spectroscopy, and x-ray diffraction. The measured dimer $(C_{60})_2$ content in the products of the polymerization of fullerite as a function of the pressure, temperature, and treatment time shows that dimerization occurs even at room temperature in the entire pressure range above $\sim$1.0 GPa. However, at least at temperatures above 400 K dimerization does not result in the formation of a dimer phase as a stable modification of the system, since the dimer is an intermediate product of the transformation. It is shown that increasing the holding time at 423 K decreases the content of the dimer fraction in the samples and results in the formation of linear (at 1.5 GPa) and two-dimensional (at 6.0 GPa) polymers, which are structure-forming elements of the orthorhombic and rhombohedral polymerized phases.
[S0021-3640(98)00624-0]

PACS numbers: 61.48.+c, 78.30.Na, 61.10.Eq

The dimer $(C_{60})_2$, which forms as a result of a $2+2$ cycloadditon reaction[1] and is the most common object of theoretical investigations among the polymerized states (PSs) of fullerene, was until very recently so inadequately studied experimentally that even the identification of the dimer molecules among other products of polymerization itself presented a substantial problem.

The point is that ordinarily the basic problems if identification of PSs can be solved by vibrational spectroscopy in combination with x-ray, electron, or neutron diffraction in cases where the PSs are crystalline. Supplementing one another, these methods of analy-

sis make it possible to determine both the structure of the polyfullerene molecules and the basic parameters of the structure of the solid formed by these molecules. Examples of the successful identification of PSs, making it possible to determine the molecular structure and the characteristic spectra of polymer molecules and to propose models of the crystal lattices, could be investigations of the orthorhombic (O), tetragonal (T), and rhombohedral (R) high-pressure phases of C_{60} fullerene,[2–8] as well as investigations of polymers observed in fullerene compounds intercalated with alkali metals.[9–11]

However, since attempts to obtain a crystalline phase based on a neutral dimer have long been unsuccessful, conclusions concerning the possibility of the existence of $(C_{60})_2$ molecules as a product of polymerization drawn on the basis of a comparison of computational[12–15] and experimental[16–18] IR and RS spectra have remained, strictly speaking, tentative. For example, on the assumption that the appearance of a line in the RS spectra at 96 cm^{-1}, attributed to the interball vibration of a dimer molecule, and the softening of the $A_g(2)$ mode to 1462–1463 cm^{-1} from the value 1469 cm^{-1} in the initial fullerite are indicative of dimer formation, it has been suggested that the dimerization of C_{60} molecules occurs both as a result of photopolymerization of fullerene at temperatures $\sim$380 K[16] and polymerization under pressure in the range 1.0–1.5 GPa and temperatures 500–700 K.[17,18]

However, samples of the pure dimer $(C_{60})_2$ and its crystal solvate with orthodichlorobenzene have recently been synthesized on the basis of mechanochemical reactions of fullerene with potassium cyanide[19,20] and then with lithium,[21] and the structure and IR[20] and RS[21] spectroscopic characteristics of the dimer molecule were determined more accurately. The appearance of clear criteria for identifying $(C_{60})_2$ molecules, requiring essentially a reexamination of the interpretation of a substantial fraction of previously obtained results on the polymerization of fullerene, made it possible at the same time to investigate the role of dimerization in these processes. The present work is devoted to the study of the role of dimerization in pressure-induced polymerization of C_{60} fullerene.

The experimental part of this work consisted in the high-pressure synthesis of various states formed by treating C_{60} fullerite at pressures up to 10 GPa, temperatures 293–623 K, and holding times from 1 to 100 000 s, separation of these states under normal conditions by quenching under pressure, and subsequent analysis of the states by x-ray diffraction and IR and RS spectroscopy. Fullerite powder with 99.9 mole % C_{60} was used as the initial material. The details of the synthesis performed using the ''Maksim'' (piston–cylinder type) and ''Toroid'' high-pressure apparatus are described in Ref. 22. The diffraction patterns were obtained on powders using an INEL CPS120 diffractometer with Cu $K\alpha 1$ radiation. The RS spectra were investigated with a Brucker FT Raman RFS100 spectrometer with an exciting laser wavelength of 1064 nm. The IR spectra of samples in the form of 0.1 mm thick potassium bromide tablets containing 3 wt. % of the product of treatment of fullerite were obtained in a Specord M 80 (Karl Zeiss) spectrophotometer.

The IR spectra in the region 400–900 cm^{-1}, which is most sensitive to the presence of interball covalent bonds, for C_{60} fullerite and the samples obtained by treatment of C_{60} fullerite at 1.5, 4.0, and 6.0 GPa pressures and room temperature are displayed in Fig. 1. According to the figure, the weak wide band at 796 cm^{-1}, observed in the spectrum of the initial fullerite (Fig. 1a), due to a symmetry-forbidden vibration in the C_{60} molecule forms even at a treatment pressure of 1.5 GPa (Fig. 1b) into a line reaching 1/3 of the

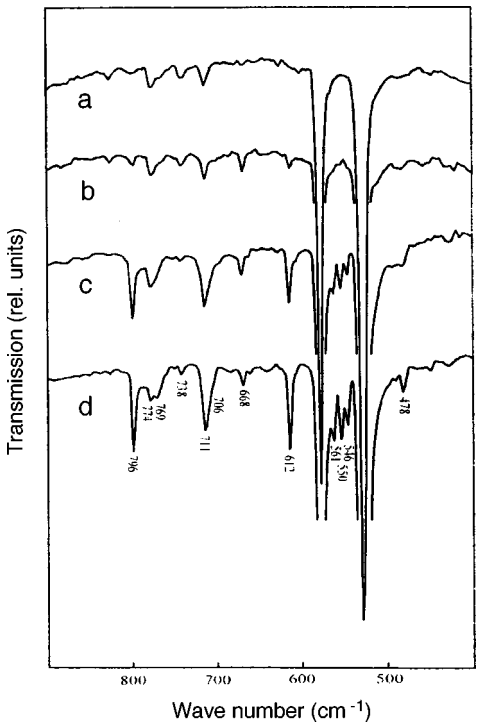

FIG. 1. IR spectra of the initial fullerite (a) and samples obtained by its treatment for 1000 s at 293 K and pressures 1.5 (b), 4.0 (c), and 6.0 (c) GPa.

intensities of the neighboring forbidden modes. A line also appears in the spectrum at 612 cm^{-1}. As the treatment pressure increases, more noticeable changes, consisting in the appearance of other bands in regions of vibrations forbidden in icosahedral symmetry and splitting of the bands (the bands at 774, 711, 561, 550, 546, and 478 cm^{-1}), are observed in the IR spectra, attesting to the lowering of molecular symmetry. The appearance of the vibration at 612 cm^{-1}, which has no analog in the C_{60} molecule, points to the formation of new covalent bonds. Comparing these results with the data of Ref. 20 shows that the main features of the spectra obtained can be explained by the formation of a dimer, whose bright characteristic lines are the lines of 796 and 478 cm^{-1}. Therefore pressure-induced dimerization of C_{60} occurs even at room temperature. It also follows from Fig. 1 that the dimer content in the experimental samples is determined by the treatment pressure.

The RS spectra are not so sensitive to the changes occurring in the system, since the 96 cm^{-1} line, which, since there are no overlappings, is more convenient to use as an analytical line for the dimer, has a comparatively low intensity. For this reason, even though the general indications of polymerization at 293 K first appear in the RS spectra of samples obtained under pressures above 2.5 GPa, in the shifts and splitting of the modes of the C_{60} molecule, and in the appearance of new vibrations (the lines at 259, 296, 515, 945, 971, 1467 cm^{-1} and others), it is difficult to draw an unequivocal conclusion about the presence of the dimer on the basis of the RS spectra even for the sample

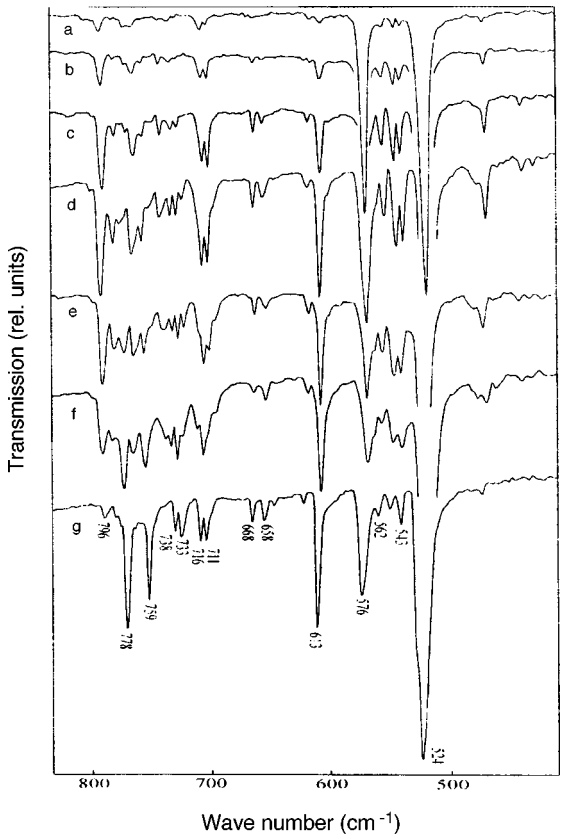

FIG. 2. IR spectra of samples obtained by treating fullerite at 1.5 GPa and 423 K for 1 (a), 10 (b), 100 (c), 1000 (e), and 50 000 s (f) and a sample (g) with O-phase content greater than 90 mole %.

treated at 6.0 GPa and containing, according to IR absorption data, $\sim$20 mole % $(C_{60})_2$.

The x-ray diffraction patterns of samples obtained at 293 K attest to the fact that dimerization of C_{60} does not produce sharp changes in the structure of the diffraction pattern as compared with the initial fullerite. The changes appear in the broadening of the diffraction peaks of the initial fullerite and a small shift of the peaks in the direction of large angles. In addition, the magnitudes of these changes are determined by the pressure and isothermal holding time. It is obvious that such an evolution of the diffraction patterns, which reflects a tendency for the average (over the system) intermolecular distance to decrease, also attests to the fact that in the solid solutions of the dimer in the monomer, which form in the first stages of the reaction, the orientation of the dimer molecules is random.

To study the possibility of obtaining a pure dimer phase on the basis of pressure-induced dimerization, the dimerization kinetics was studied for a variety of sections of the p,T diagram.

Figures 2 and 3 show the evolution of the IR spectra of samples obtained at 1.5 and 6.0 GPa as a function of the isothermal holding time at 423 K. Figures 2g and 3g also

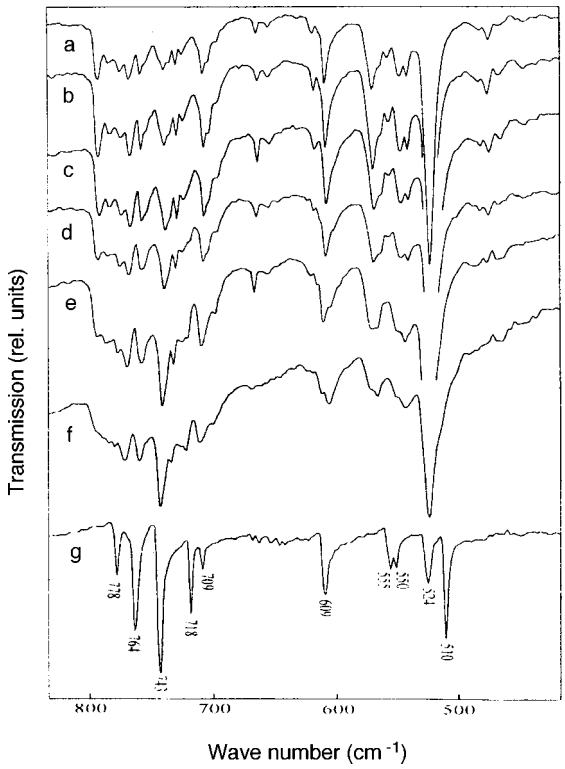

FIG. 3. IR spectra of samples obtained by treating fullerite at 6.0 GPa and 423 K for 1 (a), 10 (b), 100 (c), 1000 (d), 10 000 (e), 50 000 s (f) and a sample of the R phase (g).

display the IR spectra of samples of the O and R phases, which we obtained at 1.3 GPa, 560 K and 6.0 GPa, 900 K, respectively. It should be noted that the IR spectrum of the sample of the R phase is identical to the previously published[2,5] spectra of this phase, whereas the spectrum presented for the O phase is of the highest quality among known spectra[5] because of the high content of the O phase in the samples obtained.

According to Fig. 2, as the treatment time increases, at first the relative intensities of the dimer bands increase, indicating an increase in the $(C_{60})_2$ concentration in the samples, which reaches maximum values ($\sim$80 mole %) with holding times $\sim$1000 s. However, as the treatment time increases further, the relative intensities of the dimer peaks decrease against the background of a simultaneous increase in the intensity of the group of bands, for example at 759 and 778 cm^{-1}, characteristic for linear $(C_{60})_n$ polymers — structure-forming elements of the O phase (Fig. 2g). A similar picture of the dimer content passing through a maximum is observed in the RS spectra, since as a result of the high dimer concentration in samples obtained at 423 K, there is no longer any special difficulty in detecting $(C_{60})_2$ molecules.

The data obtained attest to the fact that at 1.5 GPa and 423 K the dimer state is not the final state, but rather it is an intermediate product of the transformation of the system. Therefore it can be inferred that for fixed p, T the stable phase is not the dimer phase but

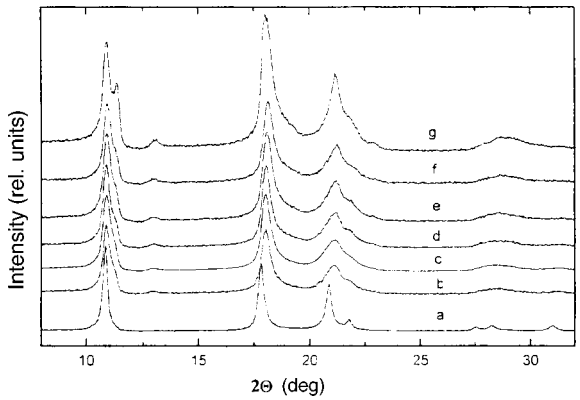

FIG. 4. X-ray diffraction patterns of the initial fullerite (a) and samples obtained by its treatment at 6.0 GPa and 423 K for 1 (b), 10 (c), 100 (d), 1000 (e), 10 000 (f), 50 000 s (g).

rather the O phase of fullerene (marked in Refs. 6–8 as O′ or ''low-pressure orthorhombic''). We note that treatment times exceeding 100 000 s are required to produce the latter in pure form under these conditions.

Analysis of the IR spectra displayed in Fig. 3 shows that the pure dimer phase likewise does not form at 6.0 GPa and 423 K. But, in contrast to the situation at 1.5 GPa, a decrease in the relative intensities of the dimer bands with increasing treatment time is accompanied by an increase in the intensities of the bands at, specifically, 743, 764, and 718 cm^{-1}, characteristic for the structure-forming elements of not the O but rather the R phase (Fig. 3g).[5] Thus, even at 6.0 GPa the dimer fraction, whose maximum concentration ($\sim$50 mole %) is obtained with treatment times of several tens of seconds, is an intermediate product of the transformation, while the final product is the R phase, even though the completion of the formation of the R phase, just as in the case of the O phase at 1.5 GPa, requires a large increase in the treatment time.

The evolution (Fig. 4) of the x-ray diffraction patterns of samples whose IR spectra are presented in Fig. 3 can serve as an illustration of the last conclusion. The diffraction patterns of samples with treatment times of 1–10 000 s attest to a large disordering in the system as a result of homogeneous dimerization of the monomer, giving rise to solid solutions with a random orientation of the dimer molecules. The crystal ordering occurring in the system as a result of the formation of the R phase is first observed as the splitting of certain peaks only with treatment times $\sim$50 000 s, although even in this case it is difficult to make an unequivocal identification of the diffraction pattern in a rhombohedral cell, and only the IR and RS spectroscopic data, which attest to the presence of structure-forming elements of the R phase in the samples, make it possible to conclude that the formation of the R phase occurs in the system.

In summary, even though the format of this letter makes it impossible to present the experimental data for other temperatures of the isobaric p,T sections at 1.5 and 6.0 GPa, they all indicate that the dimerization of C_{60} fullerene is an important stage in the evolution of the system at high pressures and temperatures, and it must therefore be taken into account both in discussions of polymerization mechanisms and in the interpretation

of previously obtained results on the identification and properties of the high-pressure states of fullerite, especially the states formed at temperatures below 623 K with short treatment times.

This work was supported by the Russian Fund for Fundamental Research (Grant No. 97-03-33584) and the INTAS Fund (Grant No. 93-2133).

*vdavydov@ns.hppi.troitsk.ru

[1] A. M. Rao, P. Zhou, K.-A. Wang *et al.*, Science **259**, 955 (1993).
[2] Y. Iwasa, N. Arima, R. M. Fleming *et al.*, Science **264**, 1570 (1994).
[3] M. Nunez-Regueiro, L. Marques, J.-L. Hodeau *et al.*, Phys. Rev. Lett. **74**, 278 (1995).
[4] C. H. Xu and G. E. Scuseria, Phys. Rev. Lett. **74**, 274 (1995).
[5] A. M. Rao, P. C. Eklund, J.-L. Hodeau *et al.*, Phys. Rev. B **55**, 4766 (1997).
[6] R. Moret, P. Launois, P.-A. Persson *et al.*, Europhys. Lett. **40**, 55 (1997).
[7] V. Agafonov, V. A. Davydov, L. S. Kashevarova *et al.*, Chem. Phys. Lett. **267**, 193 (1997).
[8] V. A. Davydov, L. S. Kashevarova, A. V. Rakhmanina *et al.* JETP Lett. **66**, 120 (1997).
[9] P. W. Stephens, G. Bertel, G. Faigel *et al.*, Nature (London) **370**, 636 (1994).
[10] Q. Zhu, D. E. Cox, and J. E. Fischer, Phys. Rev. B **54**, 11849 (1996).
[11] G. Olzlanyi, G. Bortel, G. Faigel *et al.*, Phys. Rev. B **54**, 11849 (1996).
[12] M. Menon, K. R. Subbaswamy, and M. Sawtarie, Phys. Rev. B **49**, 13966 (1994).
[13] G. B. Adams, J. B. Page, O. F. Sankey *et al.*, Phys. Rev. B **50**, 17471 (1994).
[14] D. Porezag, M. R. Pederson, Th. Frauenheim *et al.*, Phys. Rev. B **52**, 14963 (1995).
[15] D. Porezag, G. Jungnickel, Th. Frauenheim *et al.*, Appl. Phys. A: Solids Surf. **64**, 321 (1997).
[16] B. Burger, J. Winter, and H. Kuzmany, Z. Phys. B **101**, 227 (1996).
[17] P. A. Persson, U. Edlund, P. Jacobsson *et al.*, Chem. Phys. Lett. **258**, 540 (1996).
[18] V. A. Davydov, L. S. Kashevarova, A. V. Rakhmanina *et al.*, Carbon **35**, 735 (1997).
[19] G.-W. Wang, K. Komatsu, Y. Murata *et al.*, Nature (London) **387**, 583 (1997).
[20] K. Komatsu, G.-W. Wang, Y. Murata *et al.*, in *Recent Advances in the Chemistry and Physics of Fullerenes and Related Materials*, Vol. 4, edited by K. M. Kadish and R. S. Ruoff, Electrochemical Society, Pennington, 1997, p. 291.
[21] S. Lebedkin, A. Gromov, S. Giesa *et al.*, Chem. Phys. Lett. **285**, 210 (1998).
[22] V. A. Davydov, L. S. Kashevarova, A. V. Rakhmanina *et al.* JETP Lett. **63**, 818 (1996).

Translated by M. E. Alferieff

On the question of short-period oscillations of the collector voltage during transverse electron focusing

V. S. Tsoĭ*

Institute of Solid-State Physics, Russian Academy of Sciences, 142432 Chernogolovka, Moscow Region, Russia

(Submitted 11 November 1998; resubmitted 19 November 1998)
Pis'ma Zh. Éksp. Teor. Fiz. **68**, No. 12, 887–892 (25 December 1998)

Giant short-period oscillations during transverse electron focusing at high emitter voltages have been observed in bismuth samples with a superlattice on the surface. A model is proposed which explains the onset of the oscillations, their position on the magnetic-field scale, and their intensification and shift along the magnetic-field scale with increasing current (this shift depending on the direction of current flow) and which can also account for the absence of oscillations in fields which are multiples of the field of the first oscillation. In this model the oscillations are attributed to the appearance of resonant surface (edge) states and their contribution to the electron transport. © *1998 American Institute of Physics.* [S0021-3640(98)00724-5]

PACS numbers: 72.90.+y

The coherent quantum ballistics of conduction electrons determines the electric properties of a conducting mesoscopic system. Detailed information about the properties of an electronic system can be obtained with a Sharvin probe — a point contact much smaller in size than the electron mean free path l.[1] The study of quantum ballistics using a Sharvin probe in the transverse electron focusing (EF) geometry[2] makes it possible to monitor simultaneously a variety of parameters of the system, specifically, l, the Fermi momentum p_F, the character of electron reflection from the sample surface, and the surface structure.[3] Quantum ballistics effects appear in EF as, specifically, a fine structure in EF spectrum — short-period (compared with the focusing period) collector voltage oscillations as a function of the magnetic field H. Such oscillations have been observed in bismuth,[4] and later in a two-dimensional electron gas (2DEG).[5] Oscillations in bismuth have been studied in Refs. 6–9 and oscillations in 2DEG in Refs. 10–17. Evidently, there exist several types of oscillations of different physical nature. They can be conventionally divided into two groups: 1) oscillations with low excitation energies and low emitter accelerating voltages U_e, such that $eU_e \sim k_B T$ (e is the electron charge, T is the sample temperature); these oscillations can be suppressed by increasing U_e or T; 2) oscillations with high accelerating voltages, $eU_e \gg k_B T$. The oscillations observed in Refs. 4 and 5 are of the first type, while the oscillations observed in Ref. 6 are of the second type. The present letter is devoted to elucidating the physical nature of oscillations of the second type.

In most works the oscillations investigated are of the second type. Omitting the details, we shall note the general features in these works in the interpretation of the physical nature of the oscillations and the problems which arise. 1) Ballistic transit of electronic excitations with energy ~ 10 meV over distances $\geqslant 100$ μm is assumed. However, measurements of EF with intercontact spacing $\sim 5\mu$m showed that the probability of such transit is negligibly low[18] and the amplitude of the corresponding oscillations should be negligibly low, which is at variance with the measurements. 2) In principle, the oscillations can be explained by means of diffraction effects. However, the width of the EF lines in the works cited shows that the effective contact sizes >10 μm, which for the de Broglie electron wavelength in bismuth $\lambda_{dB} \sim 0.1$ μm essentially precludes diffraction by the ''aperture.'' 3) If singularities in the angular distribution of the nonequilibrium electrons injected into a sample were to arise for some reason, then as a result of specular reflection of electrons from the surface the ''lines'' due to them should also be observed in fields which are multiples of the field of the first oscillation. This is also at variance with experiment.

In the present work, to determine the physical nature of oscillations of the second type, EF measurements were performed in bismuth samples on whose surface a ''diffraction grating'' appeared spontaneously during growth. The grating was not perfect, but a distinct diffraction pattern was observed in the reflection of a laser beam from the sample surface. The average grating period estimated from the diffraction pattern was ~ 10 μm. The surface of the sample was perpendicular to $\mathbf{C}_3$ and the lines of the diffraction grating were parallel to $\mathbf{C}_1$. The emitter and collector were placed on a line parallel to $\mathbf{C}_2$. The magnetic field $\mathbf{H}$ was parallel to the surface of the sample and perpendicular to the line of the contacts. The electronic part of the Fermi surface (FS) of bismuth consists of three ellipsoids, whose major axes make a small angle with a plane parallel to $\mathbf{C}_3$. Focusing of the electrons belonging to the FS ellipsoid whose major axis was perpendicular to the line of the contacts was observed. The measurements were performed by a modulation method.[6] A dc reference current I_{0e} ($U_{0e}=I_{0e}\times R_e$, where R_e is the emitter resistance, which is independent of I_{0e} and $\mathbf{H}$) and a modulation current $I_e<1$ mA were passed through the emitter; the ac voltage U_c on the collector was measured as a function of H. The measurements were performed at liquid-helium temperatures with intercontact distances L ranging from 50 to 700 μm. Oscillations were observed in all EF spectra. A typical EF spectrum is shown in Fig. 1. As the measure of the amplitude of the oscillations that determines the scale of the effect, it is convenient to use the amplitude normalized to the amplitude of the first EF line. The influence of the observation conditions on the oscillations can be summarized as follows. 1) The number and amplitude of the oscillations were determined by uncontrollable factors and depended on the positions of both the emitter and collector. Any displacement of both the emitter and collector changed the number and amplitude of the oscillations and the position of the oscillations on the H scale. 2) In the range $L=100-700$ μm the amplitude of the oscillations could have been equal to the maximum amplitude. The specific value was determined by poorly controllable parameters that depend on the position of the contacts and not on L. 3) Oscillations were observed at both zero and relatively large values of I_{0e}. Increasing I_{0e} to 10–20 mA always increased the number and amplitude of the oscillations. However, the effect of an increase in the reference current likewise was determined by poorly controllable parameters which depend on the positions of the contacts. 4) As I_{0e} increased, the oscillations shifted in the direction of stronger fields with the polarity of U_{0e}

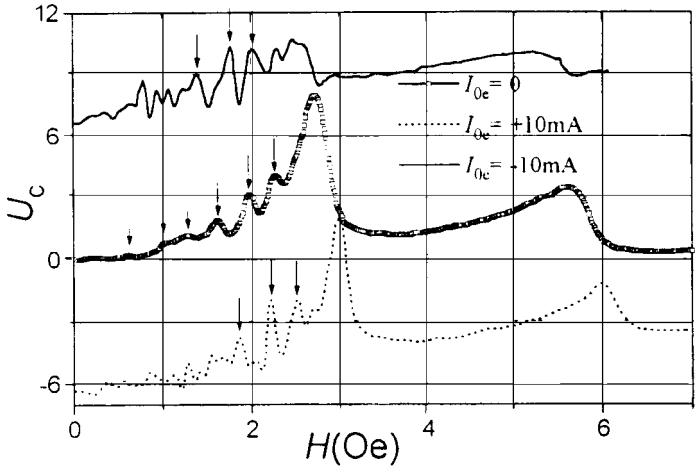

FIG. 1. Electron focusing spectra measured with $I_{0e}=0$, $+10$, and -10 mA. The distance between the contacts is 0.39 mm and $T=4.2$ K. The scale along the U_c axis is arbitrary. To reveal the details more clearly, the upper and lower curves are shifted along the U_c axis.

such that the injected electrons are accelerated. Reversing the current shifted the oscillations to weaker fields. 5) Oscillations were observed in fields $\leqslant H_0$ — the field at which the first EF line is observed — and were virtually unobserved in high fields. 6) It was virtually impossible to observe a series of oscillations in fields which were multiples of the field of the first oscillation. 7) Decreasing the temperature from 4.2 to 1.1 K ordinarily increased the relative amplitude of the oscillations.

I propose the following model which, in the Landauer–Büttiker formalism (see, for example, Ref. 19), explains all of the experimental data. In this formalism, the oscillations of the collector voltage are a consequence of the oscillations of the probability $W_{e,c}$ of electron passage from the emitter to the collector. As a result of the presence of a periodic structure on the sample surface, surface electron states (SESs) which are in resonant as a function of H appear. The oscillations in $W_{e,c}$ are due to electron transport along resonant SESs. The following are important for resonant current transmission: 1) the presence of resonant SESs, 2) trapping of the injected electrons in SESs, and 3) transition of an electron from a SES into a volume state in the collector. The high density of defects in the near-contact region of the sample makes it possible to satisfy the third condition.

The existence of SESs in bismuth is well known.[20] Under the present conditions of observation of ZF, it is virtually impossible to resolve individual SESs[4] because of the large emitter size, since the SES spectrum admits simultaneous transport along a large number of SESs with any H. Another important consequence of the large size of the contacts ($\geqslant \lambda_{dB}$) is the negligible role of the coherence of the electrons in different SESs.[5] The presence of resonant SESs radically alters the situation — for some values of H resonant electron transmission channels from the emitter to the collector open up. In the semiclassical scheme, the resonance condition is that the period of the regular surface structure is a multiple of the chord spanning the electron trajectory satisfying the quantization condition for the magnetic flux. We note that the electron flux from the emitter to

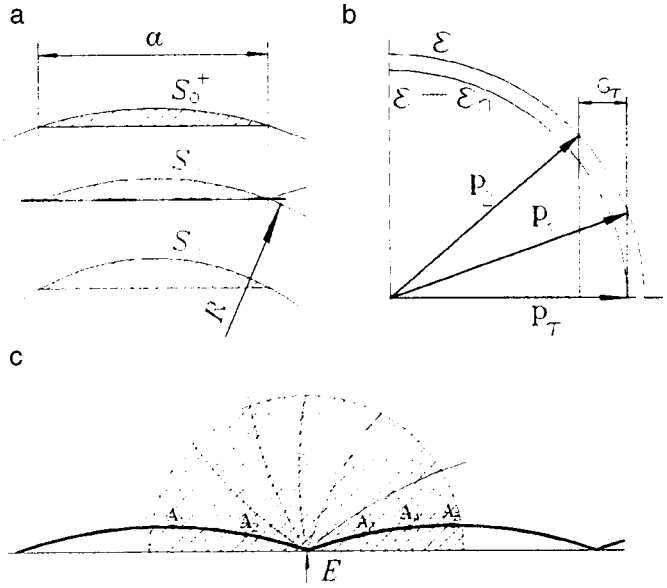

FIG. 2. a) Resonant trajectory of an electron hopping along a surface with a regular structure. The variation of the area bounded by the chord a and the arc which it spans as a function of the radius R of the circle is shown. b) Kinetics of trapping of an electron in a surface state ($\mathbf{p}_\tau$) in momentum space — from the state $\mathbf{p}_2$ with participation of the reciprocal surface-lattice vector ($\mathbf{G}_\tau \neq 0$) and from a state $\mathbf{p}_1$ with $\mathbf{G}_\tau = 0$, ϵ — electron energy in the bulk, ϵ_n — energy level of the surface state. c) The shading indicates the region of diffusion motion of nonequilibrium electrons near the emitter (E). In this region, an electron scattered, for example, at the points $A_1 - A_5$ can reach a resonant trajectory (thick line).

the collector along nonresonant SESs is suppressed as a result of the presence of a regular structure. The magnetic field $H_{n,a}$ for exciting resonant SESs is determined by the following condition (see, for example, Ref. 20): The magnetic flux threading the segment S_0 formed by an arc and the chord a spanning it (see Fig. 2a) is $\Phi = (n - \gamma)\Phi_0$, where Φ is the magnetic flux threading the segment, $n = 1,2,3,\ldots$ is the quantum number, $\Phi_0 = hc/e$ is the universal quantum of magnetic flux, and $0 < \gamma < 1$. When $H_{n+1,a} - H_{n,a}$ exceeds the width of the oscillations, the resonant levels can be observed experimentally.

Figure 3 shows a calculation of the magnetic flux threading the segment formed by an arc of the electron trajectory and the spanning chord a, $2a, 3a, 4a$, and $5a$ ($a = 30.6\ \mu$m) for electrons in bismuth. The downward arrows mark $H_{n,a}$ for $\gamma = 1/4$ with the boundary condition that the electronic wave function vanishes at the surface ($\gamma = 3/4$ with the boundary condition that the derivative of the electronic wave function vanishes at the surface).[21] The upward arrows mark the observed positions of the oscillations with $I_{0e} = 0$. The values of a and γ were chosen so as to minimize the deviation of the experimentally observed position of the three most intense oscillations with $I_{0e} = 0$ (see Fig. 1) from the computed position. For a fixed chord, suppression of the oscillations in the ES spectrum with increasing field should occur for two reasons: 1) a decrease in the distance between neighboring oscillations on the magnetic field scale and 2) a decrease in the reflection specularity due to an increase in the angle of incidence of an electron on the surface (see Fig. 2a; for SESs to exist the motion of an electron

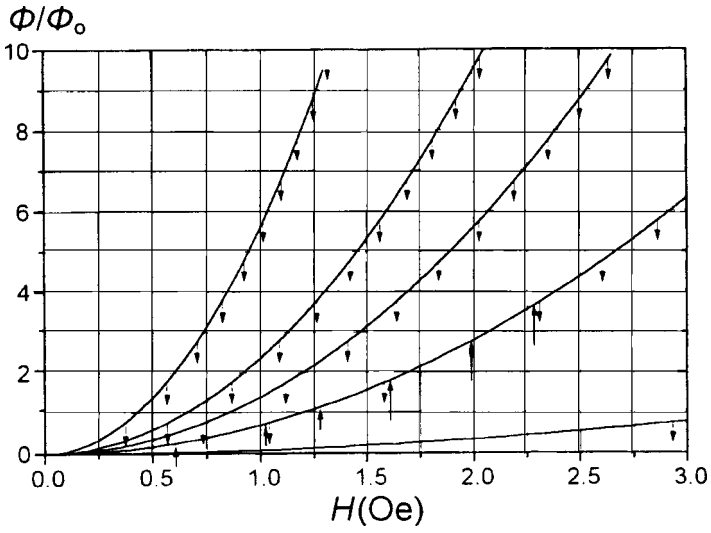

FIG. 3. The flux enclosed by the arc of an electron trajectory in bismuth and the spanning chord a, $2a$, $3a$, $4a$, $5a$ ($a=30.6$ μm) versus the magnetic field in units of the magnetic flux quantum. The downward arrows indicate $H_{n,a}$ for $\gamma=1/4$. The upward arrows mark the position of the main oscillations observed with zero dc current (see Fig. 1).

hopping along the surface must be periodic, which is possible only for specular reflection). We note that the probability of specular reflection at normal incidence is low ($\leqslant 0.4$).

Surface resonance for conduction electrons was observed in Ref. 22. The experiments were performed on bismuth samples with a surface superstructure and resonance was due to trapping of electrons in SESs. The condition for elastic trapping of an electron with kinetic energy ϵ in a SES with energy ϵ_n has the form (see Fig. 2b): $\epsilon-\epsilon_n=E_n$ and $\mathbf{p}_\tau^+=\mathbf{p}_\tau+\mathbf{G}_\tau$, where E_n is the kinetic energy of an electron in the SES in a level n, ϵ_n is the energy of the level, $\mathbf{p}_\tau^+$ and $\mathbf{p}_\tau$ are the tangential component of the momentum of an electron incident on the surface and an electron in the SES, and $\mathbf{G}_\tau$ is a reciprocal surface-lattice vector. Figure 3 shows two cases of trapping of an electron in SES: $\mathbf{p}_{1\tau}^+=\mathbf{p}_\tau(\mathbf{G}_\tau=0)$ and $\mathbf{p}_{2\tau}^+=\mathbf{p}_\tau-\mathbf{G}_\tau(\mathbf{G}\neq 0)$. For the real parameters of the problem ($\epsilon_n\sim$ several degrees, $\epsilon_F=27$ meV, period of the diffraction grating $b\sim 10$ μm), both cases are possible for grazing electrons.

If a resonant SES is excited for some value of H, then as the electron energy increases (decreases), the flux quantization condition will be satisfied in a higher (lower) field as a result of the change in the radius of the electron trajectory (see Fig. 2a), i.e., as the electron energy varies, the oscillations should shift to higher fields as energy increases or to lower fields as energy decreases. Figure 1 displays for a series of resonant SESs the computed shift of the resonant fields on the H scale as a function of the electron energy. The arrows mark the observed position of the most intense oscillations with three values of I_{0e} (see Fig. 1). One can see from Fig. 1 that in the experiment the oscillations corresponding to large values of n tend to shift in the direction of lower energies as the excitation energy of the electrons increases. This is natural because of the nonmono-

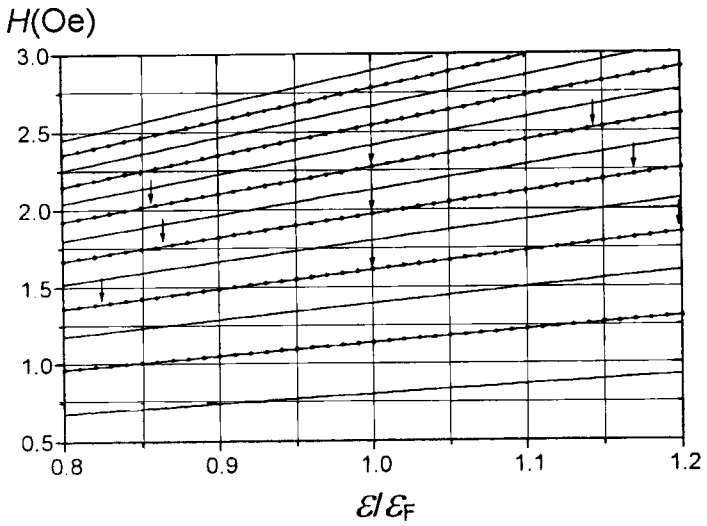

FIG. 4. Positions of the oscillations on the magnetic field scale versus the electron energy. ϵ — electron energy, ϵ_F — Fermi energy.

energetic structure of the electron beam and the exponential decrease of the contribution of the electrons as their excitation energy increases and because of the increase in the emitter-to-collector transit time of electrons with increasing n. The electron energy required by the model and determining the shift of the oscillations (see Fig. 4) agrees satisfactorily with the energy of the focused electrons with $I_{0e}=\pm 10$ mA, determined from the position of the EF line in the H scale and from the decrease of the oscillation amplitude for $L=0.39$ mm.[18]

As the emitter current increases, radical broadening of the EF line increases occurs — the effective emitter size increases (see Ref. 6 for a more detailed discussion). A zone of diffusion motion of the injected electrons appears near the emitter. In Fig. 2c, this zone is marked by hatching. The appearance of such a zone leads, specifically, to two features. 1) The probability that an electron reaches a resonant trajectory (for example, on scattering at the points A_1-A_5 in Fig. 2c) is higher than the probability in the case of ballistic flight from the emitter. An increase in the probability should result in a higher amplitude of the corresponding oscillation. 2) A possibility for additional resonant channels connecting the diffusion zone with the collector arises, and this should result in the appearance of additional oscillations with increasing emitter current. Both features, which result in an increase of the oscillation amplitude and in the appearance of additional lines in the EF spectrum, are observed experimentally (see Fig. 1).

In summary, the proposed model gives a satisfactory semiquantitative explanation of all experimental data. A detailed quantitative comparison is evidently premature, since the diffraction grating used is by no means perfect, as is indicated by the irregularity of the optical diffraction pattern obtained with the reflection of light from the surface of the experimental sample. To make a detailed quantitative analysis experiments must be performed on samples with a more perfect regular surface structure.

This work was partially supported by grants from the Russian Fund for Fundamental

Research (No. 98-02-16629) and the Ministry of Science and Technologies (No. 020/3).

*e-mail: tsoi@issp.ac.ru

[1] Yu. V. Sharvin, Zh. Éksp. Teor. Fiz. **48**, 984 (1965) [Sov. Phys. JETP **21**, 655 (1965)].
[2] V. S. Tsoĭ, JETP Lett. **19**, 70 (1974).
[3] V. S. Tsoĭ, J. Bass, and P. Wyder, Adv. Phys. **41**, 365 (1992).
[4] V. S. Tsoĭ, JETP Lett. **25**, 264 (1977).
[5] C. W. W. Beenakker, H. van Houten, and B. J. van Wees, Europhys. Lett. **7**, 359 (1988).
[6] V. S. Tsoĭ, Doctoral Dissertation [in Russian], Institute of Solid-State Physics, Russian Academy of Sciences, Chernogolovka, Russia, 1978.
[7] V. V. Andrievskiĭ, E. I. Ass, and Yu. F. Komnik, JETP Lett. **47**, 124 (1988); Fiz. Nizk. Temp. **16**, 326 (1990) [Sov. J. Low Temp. Phys. **16**, 179 (1990)].
[8] Yu. F. Komnik, V. V. Andrievskiĭ, and S. V. Rozhok, Fiz. Nizk. Temp. **22**, 1406 (1996) [Low Temp. Phys. **22**, 1066 (1996)]; Phys. Rev. B **56**, 4023 (1997).
[9] V. V. Andrievskiĭ, Yu. F. Komnik, and S. V. Rozhok, Fiz. Nizk. Temp. **22**, 1418 (1996) [Low Temp. Phys. **22**, 1076 (1996)].
[10] C. W. J. Beenakker and H. van Houten, Phys. Rev. B **39**, 10445 (1989).
[11] G. Goldoni and A. Fasolino, Phys. Rev. B **44**, 8369 (1991).
[12] A. Okiji, N. Negishi, and A. Nakamura, J. Phys. Soc. Jpn. **61**, 1145 (1992).
[13] R. I. Hornsey, J. R. A. Cleaver, and H. Ahmed, J. Vac. Sci. Technol. B **11**, 2579 (1993).
[14] T. Ueta, J. Phys. Soc. Jpn. **62**, 3633 (1993); **63**, 4506 (1994).
[15] V. J. Goldman, B. Su, and J. K. Jain, Phys. Rev. Lett. **72**, 2065 (1994).
[16] J. R. Gao, B. J. van Wees, J. J. Kuipers *et al.*, Appl. Phys. Lett. **64**, 2529 (1994).
[17] T. Ueta, J. Phys. Soc. Jpn. **64**, 4813 (1995).
[18] M. V. Tsoĭ, V. S. Tsoĭ and P. Vider, JETP Lett. **64**, 891 (1996).
[19] C. W. J. Beenakker and H. van Houten, in *Solid State Physics*, edited by H. Ehrenreich and D. Turnbull, Academic Press, New York, 1991, Vol. 44, p. 1.
[20] M. S. Khaĭkin, Usp. Fiz. Nauk **96**, 409 (1968) [Sov. Phys. Usp. **11**, 785 (1969)].
[21] A. O. F. Animalu, Philos. Mag. **21**, 137 (1970).
[22] V. S. Tsoi, Y. de Wilde, T. Noller *et al.*, Europhys. Lett. **35**, 43 (1996).

Translated by M. E. Alferieff

Ground-state instability in systems of strongly interacting fermions

S. A. Artamonov and V. R. Shaginyan
Petersburg Nuclear Physics Institute, Russian Academy of Sciences, 188350 Gatchina, Russia

Yu. G. Pogorelov
Departamento de Física, Universidade do Porto, 4150 Porto, Portugal

(Submitted 26 November 1998)
Pis'ma Zh. Éksp. Teor. Fiz. **68**, No. 12, 893–899 (25 December 1998)

The stability of a fermion system is analyzed for a model repulsive pair interaction potential. The possibility of different types of restructuring of the Fermi ground state (at sufficiently great coupling constant) is related to the analyticity properties of such potential. In particular, for the screened Coulomb law it is shown that the restructuring cannot be of the Fermi condensation type, known earlier for some exactly solvable models, but instead belongs to the class of topological transitions. A phase diagram constructed for this model in the variables ''screening parameter–coupling constant'' displays two kinds of topological transitions: a ''5/2'' kind, similar to the known Lifshitz transitions in metals, and a ''2'' kind, characteristic for a uniform strongly interacting system. © *1998 American Institute of Physics.*
[S0021-3640(98)00824-X]

PACS numbers: 71.10.Ca, 05.30.Fk

The common ground state of an isotropic Fermi gas with density ρ is described (at zero temperature) by a step-wise Fermi function $n_F(p)=\theta(p_F-p)$, which drops discontinuously from 1 to 0 at the Fermi momentum $p_F=(3\pi^2\rho)^{1/3}$ (in units where $\hbar=1$). The Landau theory of an interacting Fermi liquid starts from the assumptions that the quasiparticle distribution function $n(p)$ coincides with that of an ideal gas and that the single-particle spectrum ε_p is similar to that of an ideal gas but characterized by an effective mass M^* (Ref. 1).

However, these $n_F(p)$ and ε_p can break down under certain circumstances. The best-known example is that of Cooper pairing for an arbitrarily weak attractive interaction, with subsequent formation of the pair condensate and gapped quasiparticle spectrum,[2] but a repulsive interaction, if sufficiently strong, can also produce nontrivial ground states. The first example of such restructuring for a Fermi system with a model repulsive interaction[3] revealed the existence of a critical value $\alpha_{\rm cr}$ of the interaction constant α such that for $\alpha=\alpha_{\rm cr}$ the stability criterion $s(p)=(\varepsilon_p-\varepsilon_F)/(p^2-p_F^2)>0$ fails right at the Fermi surface: $s(p_F)=0$ (p_F instability). Then for $\alpha>\alpha_{\rm cr}$ an exact solution of a variational equation for $n(p)$ (which follows from the Landau energy functional

$E[n(p)]$) exists, exhibiting a certain finite interval (p_1,p_2) around p_F in which the distribution function $n(p)$ varies continuously and takes intermediate values between 1 and 0, while the single-particle excitation spectrum ε_p has a flat plateau,

$$\delta E[n(p)]/\delta n(p)=\varepsilon_p=\mu, \quad p_1\leqslant p\leqslant p_2, \tag{1}$$

where μ is the chemical potential. It is seen from Eq. (1) that the occupation numbers $n(p)$ become variational parameters, deviating from the Fermi function in order to minimize the energy E. This phenomenon was called fermion condensation (FC), and soon several model forms for $E[n(p)]$ were proposed[4–8] which provide similar solutions. However, these models do not answer the question of whether there exist other types of phase transitions involving a rearrangement of the Fermi function $n_F(p)$ and the single-particle spectrum ε_p. It is pertinent to note that the idea of a multiconnected Fermi sphere, with the production of new, interior segments of the Fermi surface, has been considered previously.[9,10] In this connection it is of interest to examine the overcritical regimes $\alpha>\alpha_{\rm cr}$ for models displaying alternative types of instability.

The main goal of this letter is to consider possible types of rearrangement of the Fermi ground state. We shall relate the types of such a rearrangement to the analyticity properties of the single-particle potential of a system in question and show that there can exist phase transitions of a type different from FC.

The general scheme of Refs. 3–7 for a homogeneous system of unpolarized fermions with mass M and model isotropic interaction potential $U(p)$ considers the energy functional $E[n(p)]$:

$$E[n(p)]=\int \frac{p^2}{2M}n(p)\frac{d\mathbf{p}}{(2\pi)^3}+\frac{1}{2}\int\int n(p)U(|\mathbf{p}-\mathbf{p}'|)n(p')\frac{d\mathbf{p}d\mathbf{p}'}{(2\pi)^6}, \tag{2}$$

and the related quasiparticle dispersion relation:

$$\varepsilon_p=\frac{p^2}{2M}+\int U(|\mathbf{p}-\mathbf{p}'|)n(p')\frac{d\mathbf{p}'}{(2\pi)^3}. \tag{3}$$

Performing the angular integration and passing to the dimensionless variables $x=p/p_F$, $y=2M\varepsilon_p/p_F^2$, and $z=2\pi^2ME/p_F^5$, we can present Eqs. (2) and (3) in a simpler form:

$$z[\nu(x)]=\int\left[x^4+\frac{1}{2}x^2V(x)\right]\nu(x)dx, \tag{4}$$

$$y(x)=x^2+V(x), \tag{5}$$

with the single-particle potential $V(x)$ being given by

$$V(x)=\frac{1}{x}\int x'\nu(x')u(x,x')dx', \quad u(x,x')=\frac{M}{\pi^2p_F}\int_{|x-x'|}^{x+x'}u(t)tdt. \tag{6}$$

Here $u(x)\equiv U(p_Fx)$, and the distribution function $\nu(x)\equiv n(p_Fx)$ is positive, obeys the normalization condition

$$\int x^2\nu(x)dx=1/3 \tag{7}$$

and the Pauli principle limitation $\nu(x)\leqslant 1$. The latter can be lifted using, e.g., the ansatz $\nu(x)=[1+\tanh\eta(x)]/2$; then the system ground state should correspond to the minimum of the functional

$$f[\eta(x)]=\int [1+\tanh\eta(x)]\left\{x^4-\mu x^2+\frac{1}{4}x\int x'[1+\tanh\eta(x')]u(x,x')dx'\right\}dx, \tag{8}$$

which contains a Lagrange multiplier μ, with respect to an *arbitrary* variation of the auxiliary function $\eta(x)$. This permits us to present the necessary condition of extremum $\delta f=0$ as

$$x^2\nu(x)[1-\nu(x)][y(x)-\mu]=0, \tag{9}$$

which means either that $\nu(x)$ takes only the values 0 and 1 or that the dispersion relation is flat: $y(x)=\mu$ (Ref. 3), in accordance with Eq. (1). The last possibility just corresponds to FC. As is seen from Eq. (1), the single-particle spectrum ε_p in this case cannot be an analytic function of complex p in any open domain containing the FC interval $\Delta p=[p_1,p_2]$. In fact, all the derivatives of ε_p with respect to p along Δp must be zero, while this is not the case along the real axis outside Δp. For instance, in the FC model with $U(p)=U_0/p$ (Ref. 3) the kernel, Eq. (6), turns out to be nonanalytic:

$$u(x,x')=\frac{MU_0}{\pi^2 p_F}(x+x'+|x-x'|), \tag{10}$$

which eventually causes nonanalyticity of the potential $V(x)$.

On the other hand, it follows from Eq. (5) that the single-particle spectrum will be an analytic function along the entire real axis, provided that $V(x)$ is such a function. In this case FC is forbidden, and the only alternative to the Fermi ground state (if the stability criterion gets broken) lies in a topological transition (TT) between the topologically inequivalent states with[1)] $\nu(x)=0,1$ (Ref. 11). Generally, all such states are classified by the indices of connectedness (known as Betti numbers in algebraic topology[11]) for the support of $\nu(x)$. In fact, for an isotropic system, these numbers are simply a count of the separate (concentric) segments of the Fermi surface. Then the system ground state will correspond to a multiconnected distribution (Fig. 1),

$$\nu(x)=\sum_{i=1}^{n}\theta(x-x_{2i-1})\,\theta(x_{2i}-x), \tag{11}$$

such that the parameters $0\leqslant x_1<x_2<\ldots<x_{2n}$ obey the normalization condition

$$\sum_{i=1}^{n}(x_{2i}^3-x_{2i-1}^3)=1, \tag{12}$$

and the related z, Eq. (4),

$$z=\frac{1}{2}\sum_{i=1}^{n}\int_{x_{2i-1}}^{x_{2i}}x^2[x^2+y(x)]dx, \tag{13}$$

has the absolute minimum with respect to $x_1,\ldots,x_{2n-1}$ and to $n\geqslant 1$. Differentiating Eq. (13) in the parameters $x_1,\ldots,x_{2n-1}$ with use of the relations:

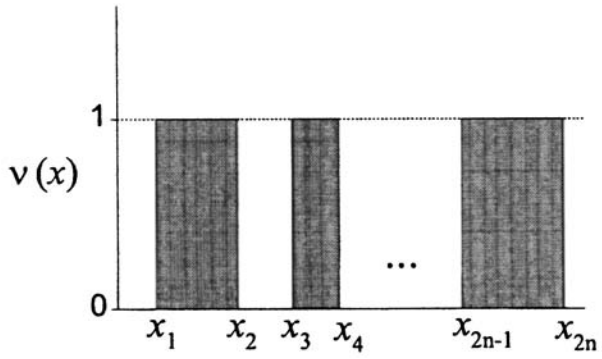

FIG. 1. Occupation function for a multiconnected distribution.

$$\partial x_{2n}/\partial x_k=(-1)^{k-1}(x_k/x_{2n})^2, \quad 1\leqslant k\leqslant 2n-1, \tag{14}$$

by virtue of Eq. (12), and taking into account that the potential $V(x)$ in the dispersion relation $y(x)$ in fact also depends on these parameters:

$$V(x)=\frac{1}{x}\sum_{i=1}^{n}\int_{x_{2i-1}}^{x_{2i}} x'u(x,x')dx', \tag{15}$$

we present the necessary conditions of extremum as:

$$\partial z/\partial x_k=(-1)^k x_k^2[y(x_k)-y(x_{2n})]=0, \quad 1\leqslant k\leqslant 2n-1. \tag{16}$$

Hence the multiconnected ground state is controlled by the obvious rule that there be a unique Fermi level: $y(x_k)=y(x_{2n})$, for all $1\leqslant k\leqslant 2n-1$ (except for $x_1=0$). In principle, given the dispersion relation $y(x)$, one can find all the $(2n-1)$ unknown parameters x_k from Eq. (16). Then, the sufficient stability conditions $\partial^2 z/\partial x_i\partial x_j=\alpha_i\delta_{ij}$, $\alpha_i>0$ lead to the generalized stability criterion: the dimensionless function,

$$\sigma(x)=2Ms(p)=\frac{y(x)-y(x_{2n})}{x^2-x_{2n}^2}, \tag{17}$$

must be positive within filled and negative within empty intervals, going to zero at their boundaries in accordance with Eq. (16). It can be proved rigorously that for a given analytic kernel $u(x,x')$, Eq. (17) uniquely determines the system ground state.

In what follows we shall label each multiconnected state, Eq. (11), by a whole number related to the binary sequence of empty and filled intervals read from x_{2n} to 0. Thus, the Fermi state with a single filled interval $[x_2=1, x_1=0]$ reads as unity, the state with a void at the origin (filled $[x_2,x_1]$ and empty $[x_1,0]$) reads as (10)=2, the state with a single gap: (101)=3, etc. Note that all even phases have a void at the origin and that the odd phases do not.

For free fermions $V(x)=0$, $y(x)=x^2$, Eqs. (16) only yield the trivial solution corresponding to the Fermi state 1. In order to pass to nontrivial realizations of TT, we choose $U(p)$ corresponding to the ordinary screened Coulomb potential:

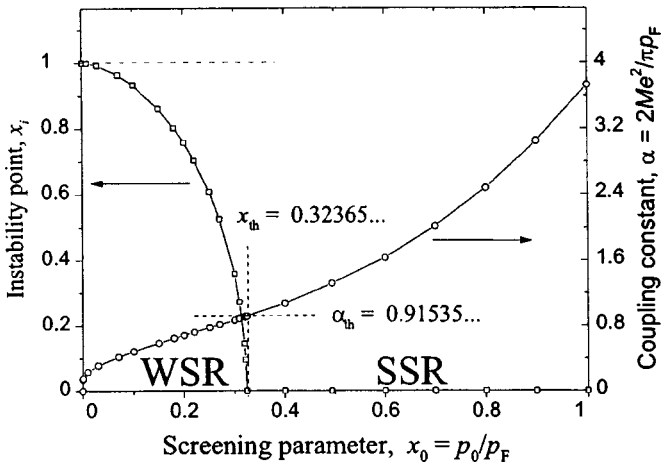

FIG. 2. Critical coupling α^* and instability point x_i as functions of screening. The regions of weak screening (WSR) and strong screening (SSR) are separated by the threshold value $x_{\rm th}$ (note that $x_{\rm th}$, $\alpha_{\rm th}$ is the triple point between the phases *1, 2, 3* in Fig. 3).

$$U(p)=4\pi e^2/(p^2+p_0^2). \tag{18}$$

The related explicit form for the kernel,

$$u(x,x')=\alpha \ln \frac{(x+x')^2+x_0^2}{(x-x')^2+x_0^2}, \tag{19}$$

with the dimensionless screening parameter $x_0=p_0/p_F$ and the coupling constant $\alpha=2Me^2/\pi p_F$, evidently displays the necessary analyticity properties for the existence of a TT. With the use of Eqs. (15) and (19), the potential $V(x)$ is expressed in terms of elementary functions as

$$V(x)=\sum_{i=1}^{n} V(x;x_{2i-1},x_{2i}), \tag{20}$$

$$V(x;x',x'')=2\alpha\left[x''-x'-x_0 \arctan \frac{2x_0(x''-x')(x^2+x_0^2+x'x'')}{(x^2+x_0^2-x'^2)(x^2+x_0^2-x''^2)}\right]$$
$$+\frac{\alpha}{2x}\left[(x''^2+x_0^2-x^2)\ln\frac{(x+x'')^2+x_0^2}{(x-x'')^2+x_0^2}-(x'^2+x_0^2-x^2)\ln\frac{(x+x')^2+x_0^2}{(x-x')^2+x_0^2}\right].$$

Then a straightforward analysis of Eq. (16) shows that their nontrivial solutions only appear when the coupling parameter α exceeds a certain critical value α^*. This corresponds to the moment when the stability criterion[3] $\sigma(x)=(y_F(1)-y_F(x))/(1-x^2)>0$ calculated with the Fermi distribution, $y_F(x)=x^2+V(x;0,1)$, fails at a certain point $0\leqslant x_i<1$ within the Fermi sphere: $\sigma(x_i)\to 0$. There are two different types of such instability depending on the screening parameter x_0 (Fig. 2). For x_0 below certain threshold value $x_{\rm th}\approx 0.32365$ (weak screening regime, WSR) the instability point x_i lies rather close to the Fermi surface: $1-x_i\ll 1$, while it falls to zero in a critical way at $x_0\to x_{\rm th}$ and

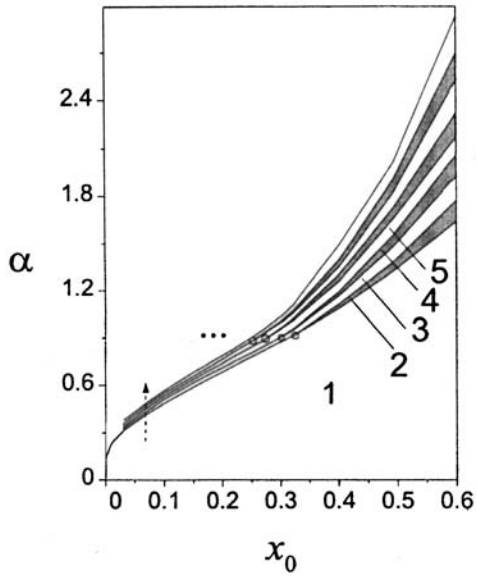

FIG. 3. Phase diagram in ''screening–coupling'' variables. Each phase with certain topology is labeled by the total number of filled and empty regions (see Fig. 1). Even phases (shaded) are separated from odd ones by lines of topological transition (TTs) of the ''$^5/_2$'' kind, while TT lines of the ''2'' kind separate odd phases. Triple points, where two TT lines of the ''$^5/_2$'' kind and one TT line of the ''2'' kind meet, are shown by circles. The dashed arrow indicates the phase trajectory studied numerically in Ref. 10.

remains zero for all $x_0 > x_{\rm th}$ (strong screening regime, SSR). The critical coupling $\alpha^*(x_0)$ results a monotonically growing function of x_0, having the asymptotic behavior $\alpha^* \approx (\ln 2/x_0 - 1)^{-1}$ at $x_0 \to 0$ and remaining analytic at $\alpha_{\rm th} = \alpha^*(x_{\rm th}) \approx 0.91535$, where it exhibits only an inflection point.

These two types of instability give rise to different types of TT from the state *1* at $\alpha > \alpha^*$: in the SSR a void appears around $x = 0$ (*1*→*2* transition), and in the WSR a gap opens around x_i (*1*→*3* transition). Further analysis of Eq. (16) shows that the point $x_{\rm th}, \alpha_{\rm th}$ represents a triple point on the phase diagram in the variables x_0, α (Fig. 3), where the phases *1*, *2*, and *3* meet. Similarly to the onset of instability in the Fermi state *1*, each TT to higher-order phases with growing α is manifested by the circumstance that $\sigma(x)$, Eq. (17), goes to zero at some point $0 \leqslant x_i < x_{2n}$ different from the existing interfaces. If this occurs at the very origin, $x_i = 0$, the phase number increases by 1 at the TT, corresponding to the opening of a void (passing from the odd to the even phase) or to the emergence of an ''island'' (even → odd). For $x_i > 0$, a thin spherical gap opens within a filled region or a thin filled spherical sheet emerges within a gap, then the phase number increases by 2, not changing the parity. A part of the whole diagram (see Fig. 3) demonstrates that with decreasing x_0 (weaken screening) all the even phases terminate at certain triple points. This agrees in particular with a numerical study of the model under consideration along the line $x_0 = 0.07$ for growing α (Ref. 10), where only the sequence of odd phases $1 \to 3 \to 5 \to \ldots$ was indicated (shown by the dashed arrow in Fig. 3).

The energy gain $\Delta(\tau)$ at the TT as a function of the small parameter $\tau = \alpha/\alpha^* - 1$ is evidently proportional to τ times the volume of a new emerging phase region

(empty or filled). Introducing the void radius δ and expanding the energy gain $\Delta(\delta) = z[n(x,\delta)] - z[n_F(x)]$ in δ, one gets $\Delta = -\beta_1 \tau \delta^3 + \beta_2 \delta^5 + O(\delta^6)$, where β_1 and β_2 are positive numbers. As a result, the optimum void radius is $\delta \sim \sqrt{\tau}$. Consequently we have $\Delta(\tau) \sim \tau^{5/2}$, which indicates a similarity of this situation to the known phase transitions of the ''$^5/_2$'' kind in the theory of metals,[12] but it has the specific property that the new segment of Fermi surface opens at very small momentum values, which can dramatically change the system response to the electron–phonon interaction, for example. On the other hand, this segment may have a pronounced effect on the thermodynamic properties of ^{3}He at low temperatures, especially in the case of P pairing, producing excitations at extremely small momenta.

For a TT with unchanged parity, the width of a gap (or a sheet) is found to be $\sim \tau$, hence the energy gain turns out to be $\Delta(\tau) \sim \tau^2$, and such a TT can be assigned to the ''2'' kind. It follows from the above consideration that each triple point in the $x_0 - \alpha$ phase diagram is a point of confluence of two TT lines of the ''$^5/_2$'' kind into one line of the ''2'' kind. The latter type of TT has already been discussed in the literature,[9,10] and we only mention here that its occurrence on a whole continuous surface in the momentum space is rather specific for systems with strong fermion–fermion interaction, while the known TTs in metals under the influence of the crystalline field occur typically at separate points in the quasimomentum space. It is of interest to note that in the limit $x_0 \to 0$, $\alpha \to 0$, reached along a line $\alpha = k x_0$, we attain the exactly solvable model: $U(p) \to (2\pi)^3 U_0 \delta(p)$ with $U_0 = k/(2Mp_F)$, which is known to display FC at all $U_0 > 0$ (Ref. 3). The analyticity mechanism of this behavior consists in the fact that the poles of $U(p)$, Eq. (18), tend to zero, thus restoring the analytic properties necessary for FC. Otherwise, the FC regime corresponds to a phase order $\to \infty$, when the density of infinitely thin filled (separated by empty) regions approaches some continuous function $0 < \nu(x) < 1$ (Ref. 10) and the dispersion relation turns flat by Eq. (16). A few remarks are in order at this point.

First, the considered model formally treats x_0 and α as independent parameters, though in fact a certain relation between them can be imposed. Under such a restriction, the system ground state should depend on a single parameter, say the particle density ρ, along a certain trajectory $\alpha(x_0)$ in the above-suggested phase diagram. For instance, with the simplest Thomas–Fermi relation for the free electron gas, $\alpha(x_0) = x_0^2/2$, this trajectory stays fully within the Fermi state *1* over all the physically reasonable range of densities. Hence a faster growth of $\alpha(x_0)$ is necessary for realization of TT in any fermionic system with the interaction (18).

Second, the single-particle potential $V(p)$ of a real system cannot be an entire function of p around p_F because of the step-wise form of the quasiparticle distribution. Therefore, as the coupling constant moves away from the critical value α^* within the WSR domain, the concentric Fermi spheres will be taken up by FC. A close look at the role of the density-wave instability, which sets in at sufficiently large α, shows that this is true.[8] In fact, these arguments do not work in the case of SSR. Thus, it is quite possible to observe the two separate Fermi sphere regimes. There is good reason to mention that neither in the case when the FC phase transition takes place nor in the case when types of TTs are present is the standard Kohn–Sham scheme[13] any longer valid. Beyond the FC or TT phase transitions the occupation numbers of quasiparticles serve as variational parameters. Thus, to get a reasonable description of the system one has to consider the ground-state energy as a functional of the occupation numbers $E[(n(p)]$ rather then a functional

of the density $E[\rho]$.[14] A more detailed study of such systems, including the finite-temperature effects, is in order.

This research was supported in part by the Portuguese program PRAXIS XXI through Project 2/2.1/FIS/302/94 and under Grant BPD 14226/97 and in part by the Russian Fund for Fundamental Research under Grant 98-02-16170.

[1)]We recall that a system with FC also presents a different topological structure (of its Green's function) from that common for ordinary Fermi liquid, marginal Fermi liquid, and Luttinger liquid.[4]

[1] L. D. Landau, JETP **30**, 1058 (1956).
[2] J. Bardeen, L. N. Cooper, and J. R. Schrieffer, Phys. Rev. **108**, 1175 (1957).
[3] V. A. Khodel and V. R. Shaginyan, JETP Lett. **51**, 553 (1990).
[4] G. E. Volovik, JETP Lett. **53**, 222 (1991).
[5] P. Nozières, J. Phys. I **2**, 443 (1992).
[6] V. A. Khodel, V. R. Shaginyan, and V. V. Khodel, Phys. Rep. **249**, 1 (1994).
[7] D. V. Khveshchenko, R. Hlubina, and T. M. Rice, Phys. Rev. B **48**, 10766 (1993).
[8] V. A. Khodel, V. R. Shaginyan, and M. V. Zverev, JETP Lett. **65**, 253 (1997).
[9] M. de Llano and J. P. Vary, Phys. Rev. C **19**, 1083 (1979); M. de Llano, A. Plastino, J. G. Zabolitsky, Phys. Rev. C **20**, 2418 (1979).
[10] M. V. Zverev and M. Baldo, http://xxx.lanl.gov/abs/cond-mat/9807324 (24 July 1998).
[11] M. Nakahara, *Geometry, Topology and Physics*, IOP Publ., Bristol (1990).
[12] I. M. Lifshitz, Sov. Phys. JETP **11**, 1130 (1960).
[13] W. Kohn and L. J. Sham, Phys. Rev. A **140**, 1133 (1965); see, also, W. Kohn and P. Vashishta, in *Theory of the Inhomogeneous Electron Gas*, edited by. S. Lundqvist and N. H. March (Plenum, New York, 1983); J. Callaway and N. H. March, Solid State Phys. **38**, 135 (1983).
[14] V. R. Shaginyan, JETP Lett. **68**, 491 (1998).

Published in English in the original Russian journal. Edited by Steve Torstveit.

Field-theoretic description of the multicritical behavior of systems with two order parameters

V. V. Prudnikov,* P. V. Prudnikov, and A. A. Fedorenko
Omsk State University, 644077 Omsk, Russia

(Submitted 21 October 1998)
Pis'ma Zh. Éksp. Teor. Fiz. **68**, No. 12, 900–905 (25 December 1998)

A field-theoretic description of phase transformations in complex systems with two interacting order parameters is given. For three-dimensional systems in the two-loop approximation a renormalization-group analysis of the scaling functions is carried out directly, and the fixed points corresponding to stability of the bicritical and tetracritical behavior are identified. The critical exponents at the multicritical points in the two-loop approximation are calculated with the use of the Padé–Borel summation technique. © *1998 American Institute of Physics.* [S0021-3640(98)00924-4]

PACS numbers: 64.60.Kw, 64.60.Ak

There exists a wide class of systems in which the observed phase transition cannot be described by one order parameter transforming according to one irreducible representation. Magnetic crystals whose magnetic structure is described by two or more irreducible representations (the antiferromagnets Cr_2TeO_6, $KCuF_3$, $GdAlO_3$, MnF_2, and others) afford exceptionally many such examples. Structural phase transitions whose description requires several order parameters have been found in $KMnF_3$, boracites, and other substances. The phase diagrams of such subsystems have a special multicritical point, which is of a bicritical or tetracritical character.[1,2] In the first case, two lines of second-order phase transitions and one line of a first-order phase transition intersect, and in the second case four lines of second-order phase transitions intersect. Close to a multicritical point the system demonstrates a specific critical behavior characterized by the competition between the different types of ordering. If bicritical behavior is realized, one order parameter in the system displaces the other, while tetracritical behavior admits the existence of a mixed phase with both types of ordering coexisting.

The model Hamiltonian of a system with two coupled order parameters ϕ and ψ, belonging to two different irreducible representations of dimension n and m, has the form

$$H_0 = \int d^dX \left(\frac{1}{2}[r_1\phi^2 + r_2\psi^2 + (\nabla\phi)^2 + (\nabla\psi)^2] + \frac{u_{10}}{4!}(\phi^2)^2 + \frac{u_{20}}{4!}(\psi^2)^2 + \frac{2u_{30}}{4!}\phi^2\psi^2 \right), \quad (1)$$

TABLE I. Values of the fixed points and eigenvalues.

$\underset{\sim}{n}$	$\underset{\sim}{m}$	u_1^*	u_2^*	u_3^*	b_1	b_2	b_3
1	1	0.93498196	0.93498196	0.93498196	0.090410	0.523089	0.667315
		1.06446157	1.06446157	0.00000000	0.653550	-0.169273	0.653550
		0.53223078	0.53223078	1.59669235	-0.205852	0.008999	0.653550
1	2	0.87048304	0.84551387	0.76415961	0.505216	0.681095	0.007546
		1.06446157	0.93498196	0.00000000	0.653550	-0.085636	0.667315
		0.82961991	0.82961991	0.82961991	-0.008388	0.474448	0.681378
1	3	1.05549842	0.82655711	0.13586107	0.016030	0.681066	0.649077
		1.06446157	0.82961991	0.00000000	0.653550	-0.019503	0.681379
		0.74314276	0.74314276	0.74314276	-0.093023	0.432386	0.695090
1	4	1.06446157	0.74314276	0.00000000	0.653550	0.695090	0.033451
		0.67140562	0.67140562	0.67140562	-0.165868	0.396007	0.708159
1	5	1.06446157	0.67140562	0.00000000	0.653550	0.076394	0.708159
		0.61123804	0.61123804	0.61123804	-0.228952	0.364435	0.720466
		0.96224764	0.65141432	-0.32221693	0.589565	-0.109812	0.728987
2	2	0.93494419	0.93494419	0.01059832	0.667270	0.667335	0.001647
		0.93498195	0.93498195	0.00000000	0.667315	-0.001673	0.667315
		0.74314276	0.74314276	0.74314276	-0.093023	0.432386	0.695090
2	3	0.93498195	0.82961991	0.00000000	0.667315	0.064781	0.681379
		0.67140562	0.67140562	0.67140562	-0.165868	0.396007	0.708159
2	4	0.93498195	0.74314276	0.00000000	0.667315	0.118008	0.695090
		0.61123804	0.61123804	0.61123804	-0.228952	0.364435	0.720466
		0.81776815	0.68640603	-0.37358192	0.555319	-0.212087	0.755115
3	3	0.82961991	0.82961991	0.00000000	0.681379	0.681379	0.131538
		0.73717819	0.73717819	-0.38320676	-0.208150	0.766734	0.545585
		0.61123804	0.61123804	0.61123804	-0.228952	0.720466	0.364435

$$\phi^2=\sum_{i=1}^{n}\phi_i^2, \quad \psi^2=\sum_{i=1}^{m}\psi_i^2, \quad (\nabla\phi)^2=\sum_{i=1}^{n}(\nabla\phi_i)^2, \quad (\nabla\psi)^2=\sum_{i=1}^{m}(\nabla\psi_i)^2.$$

The problem of a phase transition in such a system was analyzed in Ref. 3 and independently in Ref. 4. The model under consideration was investigated using Wilson's renormalization-group technique on the basis of the ϵ expansion method in the one-loop approximation. In Ref. 3, an attempt was made to trace the dependence of the character of the multicritical behavior on the numbers n and m. However, numerous investigations of systems characterized by one order parameter performed in the last few years show

that the predictions made in the one-loop approximation, especially on the basis of the ϵ expansion, can differ strongly from the real critical behavior. To shed light on this question with respect to multicritical phenomena and to determine more accurately the dependence of the character of the multicritical behavior on the structure of the order parameters, we have constructed a field-theoretic description of the system (1) in the two-loop approximation. We employed the mass theory of Ref. 5, which makes it possible to describe three-dimensional systems directly without using an ϵ expansion ($\epsilon = 4-d$, where d is the dimensionality of the system). Investigations of critical phenomena show[6] that this approach gives the best description of the critical behavior, and its application together with methods for summing asymptotically convergent series make it possible to achieve high accuracy.

As is well known, in the field-theoretic approach[7] the asymptotic critical behavior and structure of phase diagrams in the fluctuation region are determined by the Callan–Symanzik renormalization-group equation for the vertex parts of the irreducible Green's functions. To calculate the β functions and the critical exponents as functions of the renormalized interaction vertices u_1, u_2, and u_3 (scaling functions) appearing in the renormalization-group equation, we used the standard method based on the Feynmann diagram technique and the renormalization procedure.[6] As a result, we obtain for the β functions in the two-loop approximation

$$\beta_1(u_1,u_2,u_3) = -u_1 + \frac{(n+8)}{6}u_1^2 + \frac{m}{6}u_3^2 - \frac{(41n+190)}{243}u_1^3 - \frac{2m}{27}u_3^3 - \frac{23m}{243}u_1u_3^2,$$

$$\beta_2(u_1,u_2,u_3) = -u_2 + \frac{(m+8)}{6}u_2^2 + \frac{n}{6}u_3^2 - \frac{(41m+190)}{243}u_2^3 - \frac{2n}{27}u_3^3 - \frac{23n}{243}u_2u_3^2,$$

$$\beta_3(u_1,u_2,u_3) = -u_3 + \frac{2}{3}u_3^2 + \frac{(n+2)}{6}u_1u_3 + \frac{(m+2)}{6}u_2u_3 - \frac{5n+5m+72}{486}u_3^3$$
$$- \frac{23(n+2)}{486}u_1^2u_3 - \frac{23(m+2)}{486}u_2^2u_3 - \frac{(n+2)}{9}u_1u_3^2 - \frac{(m+2)}{9}u_2u_3^2, \tag{2}$$

and for the scaling functions η and γ

$$\eta_1(u_1,u_2,u_3) = \frac{2}{243}((n+2)u_1^2 + mu_3^2), \quad \eta_2(u_1,u_2,u_3) = \frac{2}{243}((m+2)u_2^2 + nu_3^2); \tag{3}$$

$$\gamma_\phi^2(u_1,u_2,u_3) = \frac{n+2}{6}u_1 + \frac{m}{6}u_3 - \frac{n+2}{18}u_1^2 - \frac{m(n-m+2)}{36}u_3^2$$
$$+ \frac{m(n+2)}{36}u_1u_3 - \frac{m(m+2)}{36}u_2u_3,$$

$$\gamma_\psi^2(u_1,u_2,u_3)=\frac{m+2}{6}u_2+\frac{n}{6}u_3-\frac{m+2}{18}u_2^2-\frac{n(m-n+2)}{36}u_3^2$$
$$+\frac{n(m+2)}{36}u_2u_3-\frac{n(n+2)}{36}u_1u_3. \quad (4)$$

It is well known that perturbation series are asymptotically convergent, and the interaction vertices of the fluctuations of the order parameters in the fluctuation region $r_1=r_2\to 0$ are large enough so that expressions (2)–(4) can be used directly. For this reason, to extract the required physical information from the expressions obtained, we employed the generalized Padé–Borel method for summing asymptotically convergent series. The direct and inverse Borel transformations extended to the multiparameter case and preserving the symmetry of the system have the form

$$f(u_1,u_2,u_3)=\sum_{i,j,k} c_{ijk}u_1^iu_2^ju_3^k=\int_0^\infty e^{-1}F(u_1t,u_2t,u_3t)dt,$$

$$F(u_1,u_2,u_3)=\sum_{i,j,k}\frac{c_{ijk}}{(i+j+k)!}u_1^iu_2^ju_3^k. \quad (5)$$

A series in the auxiliary variable λ is introduced for analytical continuation of the Borel transform of the function:

$$\tilde{F}(u_1,u_2,u_3,\lambda)=\sum_{k=0}^{\infty}\lambda^k\sum_{i=0}^{k}\sum_{j=0}^{k-i}\frac{c_{i,j,k,k-i-j}}{k!}u_1^iu_2^ju_3^{k-i-j}, \quad (6)$$

to which the $[L/M]$ Padé approximation is applied at the point $\lambda=1$. We used the $[2/1]$ approximant to calculate the β functions in the two-loop approximation. The nature of the multicritical behavior is determined by the existence of a stable fixed point satisfying the system of equations

$$\beta_k(u_1^*,u_2^*,u_3^*)=0 \quad (k=1,2,3). \quad (7)$$

The values obtained for the fixed points by solving the system (7) for the most interesting values of the number of components n and m of the order parameters are presented in Table I. The requirement that the fixed point be stable reduces to the condition that the eigenvalues b_1, b_2, and b_3 (see Table I) of the matrix

$$B_{ij}=\frac{\partial\beta_i(u_1^*,u_2^*,u_3^*)}{\partial u_j} \quad (8)$$

lie in the right-hand complex half plane.

In Ref. 3, three types of stable fixed points corresponding to different values of n and m were found. The regions of existence of these fixed points in the (n,m) plane in the one-loop approximation are shown in Fig. 1a. The type 1 corresponds to an isotropic fixed point, where $u_1^*=u_2^*=u_3^*$ and the Hamiltonian (1) is effectively the same as the Hamiltonian of a system with one $(n+m)$-component order parameter with the complete symmetry $SO(n+m)$ higher than the $SO(n)\times SO(m)$ symmetry of the initial system (manifestation of the fluctuation-determined asymptotic symmetry at the multicritical point). For points of the type 2, all three values of u_i^* are nonzero and could be different

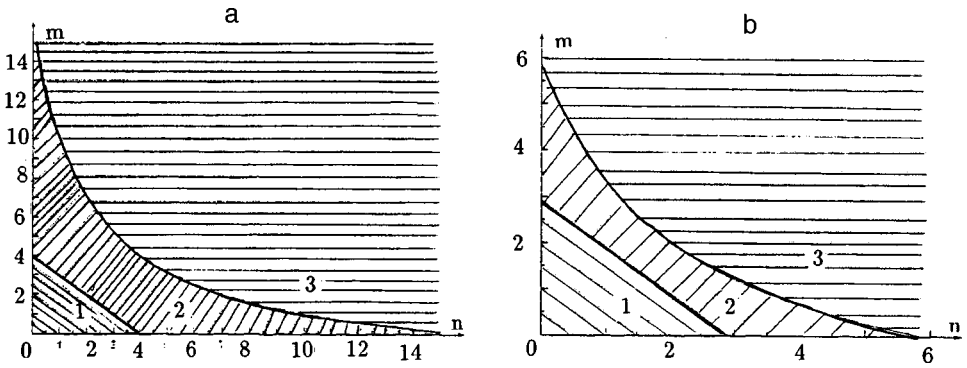

FIG. 1. Regions of stability of fixed points determined: a) in Refs. 3 and 4 in the first order of the ϵ expansion, and b) in the present letter in the field-theoretic approach in the two-loop approximation with $d=3$.

from one another. They correspond to the lowest symmetry $SO(n)\times SO(m)$ of the initial Hamiltonian. The type-3 points correspond to decoupled order parameters, since at these points $u_3^*=0$. They also correspond to the higher symmetry $SO(n)\oplus SO(m)$. Figure 1b shows the regions of existence of different types of fixed points, which we obtained in the two-loop approximation without using the ϵ expansion. The boundary of the region of stability of an isotropic fixed point now passes along the straight line $n+m=2.9088$, i.e., the highest asymptotic symmetry of the system is $SO(2)$, and the region of existence of type-2 points has become so narrow that it contains only five points of physical interest. The large change in the picture indicates that the correspondence between the one-loop approximation and the real multicritical behavior is weak.

The phase diagrams for the Hamiltonian (1) in the mean-field approximation (neglecting fluctuations) are well known.[3,8] In the case $u_3^2<u_1u_2$, a tetracritical point is realized, and therefore a mixed phase with $\phi\neq 0$ and $\psi\neq 0$ can exist. In the opposite case, $u_3^2\geqslant u_1u_2$, the phase diagram possesses a bicritical point and a mixed phase does not arise. However, as shown in Ref. 3, taking account of fluctuations can greatly change the character of the phase diagram in the critical region. For this, the phase portrait of the system must be investigated by solving the system of equations ($r=r_1=r_2$)

$$r\frac{\partial u_k}{\partial r}=\beta_k(u_1^*,u_2^*,u_3^*), \tag{9}$$

which gives the phase trajectories in the space of the vertices u_k. In the limit $r\to 0$, depending on the initial values $u_k^{(0)}$ of the vertices, the phase trajectories either leave the region of stability of the Hamiltonian (1) with the realization of a first-order phase transition or arrive at a stable fixed point from the set of fixed points examined above with a definite symmetry of the system. The phase trajectories can cross regions where the condition of tetra- or bicriticality holds for the vertices. As a result, inclusions of curves of first-order phase transitions and a set of critical points appear in the critical region in the phase diagrams corresponding to the mean-field theory.[3]

The more accurate determination made in the present letter of the values and type of the stable fixed points does not materially change the analysis of the phase portrait and phase diagrams performed in Ref. 3 for the case $n=m=1$. However, in the cases with

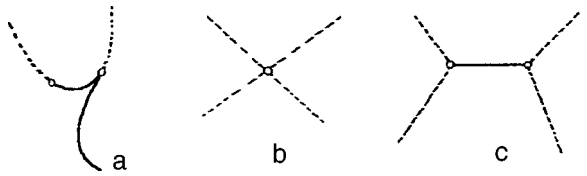

FIG. 2. Possible types of phase diagrams. The solid lines correspond to curves of first-order phase transitions and the dashed lines correspond to second-order transitions.

$n+m>2.9088$ the large change found in the values of the fixed points and their stability conditions should appreciably change the phase diagrams in the critical region and should lead to other forms of symmetry of the system at the multicritical point. As one can see from the values of u_k^* presented in Table I, the stable fixed points for $n+m\geqslant 3$ are tetracritical, i.e., $u_3^2<u_1u_2$. For this reason, if the initial values of the vertices satisfy the bicriticality condition, then the phase trajectories will always leave the region of stability of the Hamiltonian (1) and the phase diagrams that are bicritical outside the critical region will contain inclusions of curves of first-order phase transitions in the critical region (Fig. 2a). However, if the initial values of the vertices satisfy the tetracriticality condition, then for type-3 fixed points the phase diagrams are of a tetracritical character both outside and inside the critical region (Fig. 2b). The computed values of the critical exponents characterizing the tetracritical behavior are presented in Table II. The two sets of exponents for systems with $n\neq m$ reflect the fact that the critical behavior of the two

TABLE II. Values of the critical exponents.

n	m	i	η	ν	α	β	γ
1	1	-	0.02878	0.67371	-0.02114	0.34655	1.32804
1	2	1	0.02832	0.70402	-0.11206	0.36198	1.38810
		2	0.02834	0.70461	-0.11383	0.36229	1.38925
1	3	1	0.02796	0.66129	0.01613	0.33989	1.30409
		2	0.02827	0.71516	-0.14547	0.36769	1.41010
1	4	1	0.02798	0.63796	0.08613	0.32790	1.25807
		2	0.02727	0.73165	-0.19495	0.37580	1.44335
1	5	1	0.02798	0.63796	0.08613	0.32790	1.25807
		2	0.02597	0.75502	-0.26505	0.38731	1.49042
2	2	-	0.02878	0.67521	-0.02563	0.34732	1.33099
2	3	1	0.02878	0.67371	-0.02114	0.34655	1.32804
		2	0.02832	0.70474	-0.11423	0.36235	1.38953
2	4	1	0.02878	0.67371	-0.02114	0.34655	1.32804
		2	0.02727	0.73165	-0.19495	0.37580	1.44335
3	3	-	0.04532	0.93429	-0.80288	0.48832	1.82625

different order parameters can be determined independently in different experiments. However, the critical behavior of the specific heat of a system is determined by the large exponent. For type-2 fixed points, analysis of the phase portrait of the system shows that phase diagrams of two kinds are possible: They are tetracritical outside the critical region, and within the critical region diagrams of the first kind have a tetracritical point (Fig. 2b) while diagrams of the second kind contain inclusions of a curve of a first-order phase transition with two bicritical points (Fig. 2c).

In closing, we hope that the characteristic features revealed here of the multicritical behavior will find applications in the analysis of experimental works on the multicritical behavior of systems with competing order parameters.

These investigations are supported by the Russian Fund for Fundamental Research (Grant No. 97-02-16124).

*e-mail: prudnikov@univer.omsk.su

[1] K. S. Aleksandrov, A. T. Anistratov, B. V. Beznosikov, and N. V. Fedoseeva, *Phase Transitions in Crystals of Halide Compounds ABX_3*, Nauka, Novosibirsk, 1981.
[2] Y. Shapira, in *Multicritical Phenomena*, Plenum Press, New York, 1984, p. 35.
[3] I. F. Lyuksyutov, V. L. Pokrovskiĭ, and D. E. Khmel'nitskiĭ, Zh. Éksp. Teor. Fiz. **69,** 1817 (1975) [Sov. Phys. JETP **42**, 923 (1975)].
[4] J. M. Kosterlitz, D. R. Nelson, and M. E. Fisher, Phys. Rev. B **13**, 412 (1976).
[5] G. Parisi, J. Stat. Phys. **23**, 49 (1980).
[6] E. Brezin, J. C. Le Guillou, and J. Zinn-Justin, in *Phase Transitions and Critical Phenomena*, edited by C. Domb and M. S. Green, Academic Press, New York, 1976, Vol. 6, p. 125.
[7] D. Amit, *Field Theory, the Renormalization Group, and Critical Phenomena*, McGraw-Hill, New York, 1978.
[8] Yu. A. Izyumov and V. N. Syromyatnikov, *Phase Transitions and the Symmetry of Crystals* [in Russian], Nauka, Moscow, 1984.

Translated by M. E. Alferieff

In memory of our authors

S. G. Popov *et al.*, ''Investigation of the reaction $D(e,pp)e'\pi^-$ on a tensor-polarized deuterium target at high proton momenta [JETP Lett. 67, No. 10, 770–776 (25 May 1998)]

The well-known experimental physicist Professor Stanislav Georgievich Popov (1937–1996), Doctor of Physico-Mathematical Sciences, performed all of his scientific, professional, and public work in association with the G. I. Budker Institute of Nuclear Physics, Siberian Branch of the Russian Academy of Sciences.

After completing the course of study at the Department of Physics at Moscow State University, he immediately took part in the work on starting up the first colliding-beam facility in the world (VÉP-1). Next, he participated in the first experimental work on colliding beams to check the applicability of quantum electrodynamics at short distances, the observation of double bremsstrahlung, and other work.

The main phase of S. G. Popov's work was concerned with the development and application of ultrathin internal gas targets in storage rings. This method, first implemented under his direction at the Institute of Nuclear Physics, Siberian Branch of the Russian Academy of Sciences, opened up a promising new direction in experimental nuclear physics and is now used in many laboratories in the world. A series of pioneering experiments on the study of light nuclei, where the scattered electron was detected in coincidence with the reaction products, was conducted on the basis of this method at the Institute of Nuclear Physics, Siberian Branch of the Russian Academy of Sciences. Experiments performed by S. G. Popov on the study of the electromagnetic properties of the deuteron using a polarized target were especially important.

Simultaneously with his scientific work, S. G. Popov served as Scientific Secretary of the Institute and conducted active teaching work at the Novosibirsk State University.

Stanislav Georgievich Popov left a deep impression in the memories of all who worked with him.

H. Luetgemeier *et al.*, ''Electronic phase separation in a low-temperature tetragonal phase of lanthanum–strontium cuprates according to ^{139}La NQR data [JETP Lett. 67, No. 5, 363–368 (10 March 1998)]

Hans Luetgemeier, a well-known scientist in the field of nuclear magnetic resonance, died on June 12, 1997. During a large part of his career he worked at the Institute of Solid-State Research at the Science Center in Jülich. During his career he was able to create a laboratory which is widely known among scientists concerned with the problems of magnetism. He published a large number of works on various applications of nuclear magnetic resonance for deciphering the structure of matter. They include one of the first reports of the observation of nuclear quadrupole resonance in high-temperature superconductors. These works have found a large number of followers in many countries. H. Luetgemeier was one of the pioneers of German–Russian collaboration in the field of high-temperature superconductivity.

0021-3640/98/68(12)/2/$15.00

M. A. Teplov *et al.*, ''Stripe motion in CuO_2 planes of $Y_{1-x}Pr_xBa_2Cu_3O_7$ as observed from the Cu(2) quadrupole resonance'' [JETP Lett. 65, No. 10, 821–827 (25 May 1997)]

Mikhail Aleksandrovich Teplov, member of the Scientific Council on Magnetism of the Russian Academy of Sciences, head of the Department of Quantum Electronics and Radio Spectroscopy, Scientific Director of the Scientific-Research Laboratory of Magnetic Radio Spectroscopy and Quantum Electronics, and Professor at Kazan State University, died suddenly on June 13, 1998 at the age of 60. M. A. Teplov's scientific work was devoted mainly to radiospectroscopic investigations of a special class of rare-earth compounds — van Vleck paramagnets — at low and ultralow temperatures. During the last eleven years of his life M. A. Teplov worked on problems of high-temperature superconductors. The group that he directed performed the first investigations of enhanced NMR on Pr and Tm nuclei in Y–Ba–Cu–O compounds, supplementing them later with original measurements of nuclear relaxation and the width and shape of the NMR/NQR line of copper. M. A. Teplov was selflessly devoted to science and was concerned daily with the education of young scientists. He demanded much of himself, and he was principled and honest. A man of great culture, he possessed wide erudition, and he was an excellent classical musician and an expert and connoisseur of classical music.

N. I. Koroteev *et al.*, ''Spectral dependence of the excitation of the ''forbidden'' second optical harmonic in an aqueous suspension of purple membranes by femtosecond laser pulses under electronic resonance conditions'' [JETP Lett. 67, No. 4, 269–274 (25 February 1998)];

N. I. Koroteev *et al.*, ''Direct STM observation of electronic structure modification of naphthacenequinone molecules due to photoisomerization'' [JETP Lett. 68, No. 6, 521–526 (25 September 1968)];

N. I. Koroteev, ''Observation of two-step process of excitation of photoluminescence in silicon nanostructures'' [JETP Lett. 68, No. 10, 770–774 (1998)]

The eminent Russian scientist, Professor Nikolaĭ Ivanovich Koroteev, head of the Department of General Physics and Wave Processes in the Department of Physics at the M. V. Lomonosov Moscow State University, and Director of the International Teaching and Science Center for Lasers, died prematurely on December 4, 1998. Under N. I. Koroteev's leadership, the department which he headed and the International Laser Center at Moscow State University continued the scientific traditions of the nonlinear optics school at Moscow University, taking leading positions in a variety of directions in laser physics and nonlinear optics. N. I. Koroteev was a brilliant scientist and organizer of sciences, a talented teacher, and educator. Among his scientific achievements are the development of a large and fruitful field of laser spectroscopy — the spectroscopy of coherent anti-Stokes scattering — and the development of nonlinear optical methods for laser diagnostics of ultrafast processes in nonequilibrium systems.

Translated by M. E. Alferieff